Received: 23 January 2025 | Revised: 14 April 2025 | Accepted: 9 May 2025

DOI: 10.1002/qj.5025

Quarterly Journal of the Royal Meteorological Society RMetS

RESEARCH ARTICLE

A consistent coupling of two-moment microphysics and bulk ice optical properties, and its impact on radiation in a regional weather model

Anthony J. Baran[1,2] | **James Manners**[1] | **Paul R. Field**[1,3] | **Kalli Furtado**[4] | **Adrian Hill**[5]

[1]Met Office, Exeter, UK

[2]School of Physics, Astronomy and Mathematics, University of Hertfordshire, Hatfield, UK

[3]Institute for Climate and Atmospheric Science, School of Earth and Environment, University of Leeds, Leeds, UK

[4]Meteorological Service Singapore, Centre for Climate Research Singapore, Singapore, Singapore

[5]European Centre for Medium-Range Weather Forecasts, Reading, UK

Correspondence
Anthony J. Baran, Met Office, FitzRoy Road, Exeter, Devon, EX1 3PB, UK.
Email: anthony.baran@metoffice.gov.uk

Abstract

We present a consistent coupling between two-moment microphysics and bulk ice optics in the Met Office's 1.5-km resolution regional weather model and study its impact on top-of-atmosphere (TOA) short- and long-wave irradiances. The coupling links the prognostic moments (total mass and number) to bulk ice optical properties through the mass-equivalent spherical radius using Padé approximants. Model runs were evaluated for Darwin, Australia (January–March 2017) and the UK (December 2017–March 2018). Using this consistent coupled parametrisation, we demonstrate improved simulation of TOA short-wave irradiances over both regions compared to the non-consistent ice optical parametrisation when validated against satellite observations. Similar improvements were found for TOA long-wave irradiances over Darwin, though the consistent parametrisation was slightly too transmissive over the UK. Overall, our more consistent two-moment coupling between microphysics and ice optics leads to generally better prediction of radiation fields than single-moment parametrisations.

KEYWORDS

regional modelling, remote sensing, snow

1 | INTRODUCTION

The Intergovernmental Panel on Climate Change (IPCC) has long highlighted the lack of understanding of the radiative coupling of clouds to the atmosphere, notably in their 2021 report and earlier assessments. This gap in knowledge exacerbates the significant uncertainty in predicting the Earth's climate equilibrium, as summarised by Stocker *et al.* (2013). The primary driver of this uncertainty is the cloud radiative feedback effect, as discussed by Boucher *et al.* (2013) and Sherwood *et al.* (2020). These uncertainties arise partly from the differing cloud physics assumptions within the various models used for the IPCC assessments and are closely related to present-day biases in cloud properties predicted by climate models, see for example Rostron *et al.* (2020), Ceppi and Nowack (2021), Furtado *et al.* (2023), and Jiang *et al.* (2023).

Ice crystal clouds, or cirrus, significantly contribute to the uncertainty in the sign of the radiative feedback. These clouds can either cool or warm the planet's surface depending on their macrophysical and microphysical states (Baran, 2012; Liou, 1986; Yang *et al.*, 2015; Zhang *et al.*, 1999). Overall, cirrus clouds are observed to contribute to a net warming effect of about $5.1 \pm 3.1\,\mathrm{W\,m^{-2}}$ (Hong *et al.*, 2016). However, this value has significant uncertainty due to the differing treatments of ice crystal particle size distributions (PSDs) and ice crystal habits in the satellite retrievals used to estimate the net radiative effect of cirrus.

These differences in cirrus microphysics also manifest themselves within the models used in the IPCC assessments, contributing to the intermodel differences mentioned earlier. Furthermore, the microphysics and radiative parametrisations of cirrus within models can impact the prediction of low clouds due to the vertical profile of heating, as shown by McFarquhar *et al.* (2003). The processes of scattering and absorption by atmospheric ice crystals are crucial to the vertical profile of heating within cirrus (Yang *et al.*, 2012; Zhao *et al.*, 2018) and to their short-wave and long-wave radiative properties (Baran, 2009; Yang *et al.*, 2015). However, depending on the ice crystal model adopted for the scattering and absorption properties, there can be substantial differences for the radiative simulations of cirrus in general circulation models (GCMs) and for satellite retrievals of cirrus properties; see for instance the works of Edwards *et al.* (2007), Yang *et al.* (2012), Yang *et al.* (2013), Baran, Hill, *et al.* (2014b), Zhao *et al.* (2018), Ren *et al.* (2021), and Ren *et al.* (2023).

To quantify and constrain the net radiative effect of cirrus, it is essential to construct accurate parametrisations of their bulk optical properties. However, as many studies have shown, there is yet to be a consensus on which ice crystal model of bulk ice optical properties is best to apply in GCMs and/or remote sensing. Given the variety of scattering models that exist (see for instance Baran, Cotton, *et al.*, 2014a; Baum *et al.*, 2011; Eriksson *et al.*, 2018; Kleanthous *et al.*, 2024; Li *et al.*, 2022; Yang *et al.*, 2013), ensuring some level of consistency between the GCM's microphysics and radiation schemes is crucial. This is usually achieved by ensuring that the PSDs, the mass dimension of the ice crystal model, or the characteristic dimensions of the PSDs are consistent between the two schemes (Bae *et al.*, 2016; Baran *et al.*, 2016; Baran, Hill, *et al.*, 2014b; Ren *et al.*, 2021; Ren *et al.*, 2023; Zhao *et al.*, 2018). The recent study by Ren *et al.* (2023) emphasises the importance of consistency in ice cloud optical models when applied to remote sensing and broadband radiative transfer simulations. They note that inconsistent ice optical properties can lead to systematic errors when calculating cloud radiative effects, and these errors exceed the observational uncertainties. The authors advocate the further development of more microphysically and optically consistent ice crystal models such as the Baran, Cotton, *et al.* (2014a) and the Liu *et al.* (2014) two-habit mixture model approaches. In a previous study by Bae *et al.* (2016), they demonstrated improved agreement with observed short-wave irradiances reaching the ground and precipitation patterns by consistently coupling the Weather Research Forecasting (WRF) two-moment six-class (WDM6) microphysics scheme with the radiation scheme. This was achieved by dynamically calculating the characteristic dimension of the PSD for hydrometeors based on their number and mass concentrations. The works of Baran, Hill, *et al.* (2014b), Bae *et al.* (2016), and Ren *et al.* (2023) demonstrate the importance of consistently linking the microphysics and radiation schemes in weather and climate models to improve their representation of radiation processes.

The characteristic dimensions of the PSDs in radiation schemes are commonly defined in terms of the effective dimension, D_e, which is the mean particle size weighted by the projected area of the randomly oriented ice crystal or the ratio between the ice water content (IWC) and the volume extinction coefficient (Foot, 1988; Francis, 1995; McFarquhar & Heymsfield, 1998; Mitchell, 2002). However, studies by Francis (1995), Baran (2012), Baran, Hill, *et al.* (2014b), Baran *et al.* (2016), and Sieron *et al.* (2017) have pointed out shortcomings in using effective dimension-based methods to describe the single-scattering properties of ice crystals. Notably, ice crystals, being approximately fractal in nature as they aggregate, will have mass and area dimensions that tend to fractal dimensions of nearly two or less than two, respectively (Field *et al.*, 2008; Westbrook *et al.*, 2004). Since D_e is a ratio between mass and area, it becomes much less radiatively impactful as the ice crystals aggregate with distance from the cloud top. For this reason, Baran, Hill, *et al.* (2014b) and Baran *et al.* (2016) developed a consistent coupled cirrus microphysics–radiation parametrisation that relates the bulk ice optical properties directly to the IWC and in-cloud temperature. This parametrisation maintains consistency between the cirrus microphysics and radiation schemes through the IWC and PSDs, where the latter is based on the Field *et al.* (2007) moment estimation parametrisation of the PSD, generated through the mass–dimension relation derived by Cotton *et al.* (2013) and the in-cloud temperature.

Interestingly, Zhou *et al.* (2024) explore the characteristics of the Fengyun-4A Advanced Geostationary Radiation Imager visible reflectance data and evaluate uncertainties due to model errors. A notable focus of the study includes sensitivity analyses of radiances simulated with ice cloud optical property parametrisations based on those provided by Baran, Cotton, *et al.* (2014a), hereinafter referred to as Baran, and Baum *et al.* (2011), hereinafter referred to as Baum. The study shows systematic differences between the two parametrisations when used to simulate the visible reflectance of ice clouds, with the Baran parametrisations generally giving higher reflectance values than the Baum approach. This indicates that these parametrisation differences are major contributors to uncertainties in ice cloud radiative properties. However, the authors noted advantages in the Baran approach due to its direct link to microphysical variables rather than relying on parametrisations involving the effective radius, r_e (i.e., $r_e = D_e/2$). They found that when models do not directly predict r_e from their cloud microphysics schemes, it must be approximated, which can exacerbate forward model errors when using the Baum parametrisation. This represents a potential limitation of ice optical property parametrisations linked to r_e, which could impact their usability in radiative transfer model intercomparisons.

In an earlier study, Geiss *et al.* (2021) evaluated cloud representations in numerical weather prediction (NWP) models using visible and infrared observations and again examined differences between the Baran and Baum ice optical property representations. They found that the Baran bulk ice optical parametrisations gave consistent representation of visible reflectances for optically thin and thick ice clouds. However, the Baum parametrisations underestimated visible reflectances, especially for optically thin ice clouds, consistent with the findings of Zhou *et al.* (2024). The study highlighted the advantages of linking the bulk ice optical properties directly to the bulk IWC and temperature, as this linkage provides a more flexible framework, particularly in the absence of detailed microphysics information. However, forward model errors were dominated by differences in the schemes' ice particle shape representations, scattering assumptions, and sensitivities to subgrid-scale processes. The study found that subgrid-scale processes of clouds were a significant source of systematic errors, especially for reflectances. To minimise such errors, the authors suggest moving away from single-moment PSDs. They propose that two-moment or even higher-order PSDs could better capture natural variability in ice crystal size and concentrations, potentially reducing biases in cloud radiative property simulations.

A comprehensive comparison of the single-scattering properties between different ice optical parametrisations (such as Baran and Baum) would be valuable to quantify how much of the systematic differences in simulated radiative properties stems from the optical particle models themselves versus the use of different connecting variables (e.g., effective radius vs direct microphysical quantities). Such analysis could help isolate the specific impacts of habit assumptions, treatment of surface roughness, and other microphysical factors on radiative transfer predictions.

Clearly, the Baran ice optical parametrisations, which relate the bulk ice optical properties, IWC and in-cloud temperature, are based on a single moment. In the previous discussion, we highlighted the advantages of developing bulk ice optical property parametrisations using two-moment microphysics to reduce forward model uncertainties. Moreover, single-moment parametrisations preclude the possible occurrence of the Twomey effect (Twomey, 1977). This is because single-moment parametrisations, which predict only one moment of the hydrometeor size distribution (typically the mass mixing ratio), do not account for changes in the number concentration of cloud droplets. This limitation precludes the accurate representation of the Twomey effect. While previous studies, such as Bae *et al.* (2016), dynamically linked effective radii to radiation schemes using two-moment microphysics, these approaches rely on assumptions about effective radius that may introduce inconsistencies, as noted in the previous discussions. This study addresses these limitations by coupling two-moment microphysics directly to bulk ice optical properties, enabling more physically consistent simulations of radiation fields. This is achieved by developing a new cirrus bulk ice optical parametrisation based on two moments (i.e., ice mass mixing ratio and number) for the Met Office's two-moment microphysics scheme.

To improve the representation of multiple moment interactions in GCMs, it is crucial to model these interactions accurately at a fundamental level to better replicate subgrid-scale cloud processes. Addressing this need, Shipway and Hill (2012), Hill *et al.* (2015), and Field *et al.* (2023) developed the Met Office's Cloud and Aerosol Interaction Model (CASIM) to incorporate multiple moment effects in the in-cloud processing of atmospheric particulates. CASIM is designed to replace the current microphysics scheme used in the Unified Model and the Met Office-NERC cloud model (MONC) for long-term use (see Hill *et al.*, 2018 for details about MONC). CASIM enables the use of several species, including the number concentrations of cloud water, rain, cloud ice, snow, and graupel. Cloud ice and cloud water can be represented by one or two prognostic moments, while rain, snow, and graupel can use a third prognostic moment. These prognostic moments include number concentration, mass, and some representation of the shape of the size distribution, such as radar reflectivity.

In CASIM at the Met Office, the ice number is initiated through homogeneous freezing of water droplets and heterogeneous ice nucleation. When ice number is not initiated by aerosol, it is based on the Cooper (1986) relationship between ice number and cloud temperature, which serves as the climatological background. In this study, we use this latter method for ice number production throughout the paper. The formation of ice crystals also depends on the amount of water vapour present and temperature. CASIM predictions have been validated through several observational studies, including those by Leon *et al.* (2016), Miltenberger *et al.* (2018), and Gordon *et al.* (2020), which used the Facility for Airborne Atmospheric Measurements (FAAM) BAe-146 aircraft, though these studies mainly focused on water clouds and rain. Furtado *et al.* (2018) demonstrated that the CASIM two-moment microphysics consistently outperformed single-moment schemes in reproducing observed cloud radiative and precipitation properties. Additionally, it provided radar reflectivity distributions that aligned more closely with ground-based S-band radar observations. By combining these observations with CASIM developments, we can reduce the existing uncertainties related to the radiative effect of multimoment interactions. This unknown quantity contributes to the large uncertainty in the modelling and observational estimates of the cloud radiative effect, as highlighted in the IPCC, 2021 report and earlier reports.

It is more effective to relate model prognostic variables, such as mass and number concentration, directly to ice optical properties rather than relying on an intermediate variable like the effective radius. Effective radius is not a prognostic variable in weather and climate models and can introduce errors due to its dependence on additional assumptions. Our approach directly connects radiative transfer simulations within CASIM to radiometric observations, facilitating better evaluation against such observations and enabling a more realistic representation of radiative effects, including aerosol–ice interactions.

This paper is divided into several sections. Section 2 provides a brief overview of the ensemble model of cirrus ice crystals (i.e., the model on which the coupled consistent ice optical parametrisation is based) developed by Baran and Labonnote (2007), along with definitions of the bulk ice optical properties. In Section 3 , we describe the assumed CASIM PSD, along with the required moments and the mass assumptions used to generate the PSDs. Section 4 details the CASIM data utilised to generate the PSDs from the prognostic two-moment microphysics to develop the ice optical parametrisation. In Section 5 , we describe the fully consistent new parametrisation. Section 6 presents the Darwin, Australia, regional case study used to evaluate the performance of the new ice optical parametrisation against CERES short-wave and long-wave irradiance measurements. Results from around the UK are also presented in this section. Finally, Section 7 discusses the conclusions drawn from this paper.

2 | THE ENSEMBLE MODEL OF CIRRUS ICE CRYSTALS

The ensemble model of cirrus ice crystals was developed by Baran and Labonnote (2007) and is reproduced here as Figure 1. The figure shows that the ensemble model consists of six elements, the first of which is the hexagonal ice column with an aspect ratio of unity, and the second element is the six-branched bullet rosette. Thereafter, hexagonal monomers are arbitrarily attached to each other as a function of maximum dimension, D_{max}, forming three- to ten-element hexagonal ice aggregates. The elements are constructed so as not to contain intersecting planes, and the monomers are attached such that multiple reflections between monomers are negligible, which was determined experimentally using ray-tracing calculations. The first element represents the smaller sizes of ice crystals in the PSD, while the hexagonal ice aggregates represent the process of ice crystal aggregation and, thus, the ice crystals of larger size in the PSD. In this paper, each particle of the ensemble model is placed in PSD size bins in the proceeding order and is not weighted in any of the size bins. The shapes of each ensemble model member are shown in Figure 1.

Figure 2 shows the distribution of ensemble model members as a function of maximum dimension within each of the size ranges shown in the figure, where the distribution of each member is uniform across each of the size ranges.

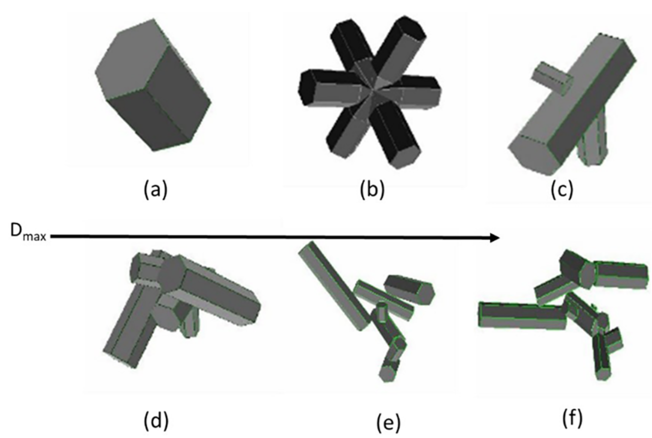

FIGURE 1 Ensemble model of Baran and Labonnote (2007) consisting of six elements that progressively increase in complexity as a function of the maximum dimension (D_{max}): (a) the hexagonal ice column with an aspect ratio of unity; (b) the six-branched bullet rosette; (c) the three-branched hexagonal aggregate; (d) the compact five-branched hexagonal aggregate; (e) the eight-element chain hexagonal aggregate; and finally (f) the 10-element chain hexagonal aggregate. [Colour figure can be viewed at wileyonlinelibrary.com]

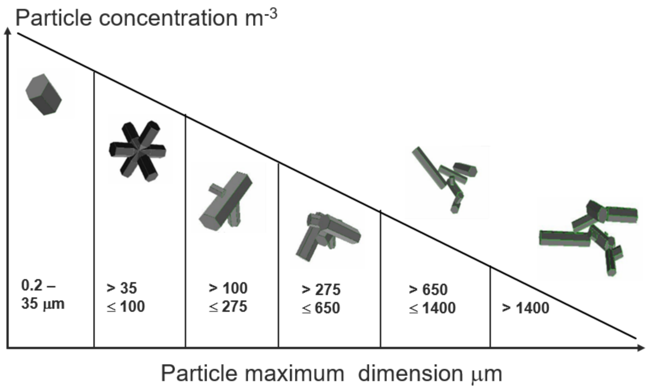

FIGURE 2 Distribution of ensemble model members from 1 to 6 plotted against the number concentration and maximum dimension of some fictitious particle size distribution. In each size range, the distribution is uniform for each of the six members. [Colour figure can be viewed at wileyonlinelibrary.com]

As depicted in Figure 2, the aggregation of ice crystals increases as the maximum dimension of particles increases. This process of increased aggregation with particle size is consistent with the observations of Field *et al.* (2008) and Lawson *et al.* (2019), as well as references cited therein. As ice crystal aggregation increases, the area ratio (that is, the ratio of the orientation-averaged projected area of the non-spherical particle to the projected area of the circumscribed sphere having the same maximum dimension as the non-spherical particle) of the aggregates tends toward a value of approximately 0.5 or less, according to Field *et al.* (2008). The ensemble model area ratio follows a similar trend to the observations as the maximum dimensions increase, and they fall within the uncertainties of the microphysics observations, as demonstrated in Baran *et al.* (2015).

The choice of habits presented in Figure 1 follows from the published literature on ice crystal aggregation and morphology found in cirrus at the time. The primary reasoning is published in Baran and Labonnote (2007, Section 3, p. 1902), which we do not repeat here for reasons of brevity. However, the hexagonal ice column shown in Figures 1a and 2 was chosen to represent smaller ice crystals (<35 μm) based on in-situ evidence from Korolev and Isaac (2003), who demonstrated that particles of size less than 30–40 μm typically exhibit aspect ratios close to unity, and these small ice crystals were not spherical in nature. The ensemble model focuses on columnar forms and their aggregates rather than plate-like crystals because, as shown, after Baran and Labonnote (2007), by Bailey and Hallett (2009), columnar aggregates dominate at temperatures below approximately −40°C, which are typical of pure ice crystal formation conditions in cirrus. The study by Bailey and Hallett (2009) has provided further observational support for the predominance of columnar aggregates at cirrus forming temperatures.

The bulk scattering properties predicted by the distribution of ensemble model members shown in Figure 2 have been evaluated against active and radiometric observations from various aircraft campaigns and multispectral satellite observations. The ensemble model predictions are within the uncertainties of the active and radiometric measurements in studies conducted by Baran, Cotton, *et al.* (2014a) and Sourdeval *et al.* (2015, 2016). More recently, Röttenbacher *et al.* (2024) provided a detailed evaluation of several ice optics parametrisations, namely Fu-IFS (Fu, 1996), Yi *et al.* (2013), and Baran *et al.* (2016), within the ecRad radiation scheme of the European Centre for Medium-Range Weather Forecasts (ECMWF; Hogan & Bozzo, 2018) for simulating solar transmissivity of Arctic cirrus. While initial comparisons using model-predicted IWC and effective radius showed only minor differences among the three parametrisations, sensitivity tests using retrieved IWC demonstrated more notable differences. Specifically, for optically thick Arctic cirrus, Fu-IFS and Yi2013 overestimated solar transmissivity, whereas Baran2016 provided slightly improved agreement with measurements. Röttenbacher *et al.* (2024) also highlighted that the Baran2016 parametrisation, based on recent in-situ ice crystal measurements and employing the moment estimation parametrisation of the PSD by Field *et al.* (2007), offers improved statistical robustness across a broad range of IWC and temperature conditions typical of the Arctic. Additionally, Baran2016 eliminates reliance on effective radius assumptions, which is considered an advantage relative to the Fu-IFS and Yi2013 schemes.

2.1 | Calculation of the bulk optical properties

SOCRATES (Suite Of Community RAdiative Transfer codes based on Edwards and Slingo) is the radiation scheme used in the Met Office's Earth and planetary science work and is described by Manners *et al.* (2023). The single-scattering properties employed in this study were calculated assuming randomly oriented ice crystals in 3D space. Thus, the calculations do not explicitly include effects due to preferential fall orientation. Here, to simulate the radiation fields, SOCRATES employs input from CASIM to solve for the outgoing irradiances via the two-stream approximation within the Edwards–Slingo radiative transfer model (Edwards & Slingo, 1996). For this purpose, only the bulk optical properties are required, since the two-stream radiative transfer approximation is employed to compute the outgoing radiation fields; these are the bulk extinction (C_{ext}), scattering (C_{sca}) and absorption (C_{abs}) coefficients, as well as the single-scattering albedo (ω_0) and the asymmetry parameter (g). The definitions of these bulk optical properties are as follows:

$$\langle C_{\mathrm{ext,sca}}\rangle = \int_{D_{\min}}^{D_{\max}} n(\bar{l}) < C_{\mathrm{ext,sca}}(\overline{l}) > \mathrm{d}\bar{l}, \tag{1}$$

where in Equation (1), $C_{\mathrm{ext/sca}}(\bar{l})$ is the orientation-averaged scattering and extinction cross-section of each of the elements in the ensemble model, the vector $\mathbf{l}$ contains each ensemble model element as a function of its size, and $n(\bar{l})$ denotes the PSD. For ease of reading, the brackets are omitted, hereinafter.

From C_{ext} and C_{sca}, the absorption cross-section can be found via

$$C_{\mathrm{abs}} = C_{\mathrm{ext}} - C_{\mathrm{sca}}, \tag{2}$$

from which the single-scattering albedo, ω_0, can be readily obtained from,

$$\omega_0 = \frac{C_{\mathrm{sca}}}{C_{\mathrm{sca}} + C_{\mathrm{abs}}}. \tag{3}$$

The co-albedo is then defined as $1 - \omega_0$.

Finally, <g> is defined as:

$$< g >= \frac{\int_{D\min}^{D\max} g(\bar{l}) C_{\mathrm{sca}}(\bar{l}) n(\bar{l}) d\bar{l}}{\int_{D\min}^{D\max} C_{\mathrm{sca}}(\bar{l}) n(\bar{l}) d\bar{l}}. \tag{4}$$

In Equation (4), all the terms have been defined previously. Equations (1)–(4) are employed to calculate the ensemble model's bulk optical properties at 170 wavelengths between the wavelengths of 0.175 and 100 μm.

The wavelength resolution used to compute the ensemble model bulk optical properties is shown in Figure 3a,b. The figures show the real and imaginary indices of solid ice, as compiled by Warren and Brandt (2008), with open circles superimposed on the refractive indices representing the wavelengths at which the bulk optical properties are calculated. From the figures, it is evident that the wavelength resolution used in this paper is adequate to capture the rapid variations in the ice refractive index, particularly between 1.5 μm and 4.0 μm, and at wavelengths in the terrestrial window and far-infrared regions.

The calculation of the single-scattering properties of each of the ensemble model members between the wavelengths of 0.175 and 100 μm is now described and follows the description in Baran, Cotton, *et al.* (2014b). At wavelengths between 0.2 and 4.9 μm, the total optical properties (i.e., the integral optical properties, given by Equations 1–4) were calculated using the Monte Carlo ray-tracing method developed by Macke *et al.* (1996); each element of the ensemble is randomised using the method of distortion, and maximum randomizations are achieved using distortion and include ice crystals with spherical air bubbles. The method of distortion is described in Macke *et al.* (1996); however, a brief description of the method is given here. For every reflection and refraction event at the interface of a convex facet, the tilt angle, θ_t, is randomly varied while a uniform probability density function is assumed. This changes the directions of the ray paths, which has the effect of removing energy from the halo and ice bow regions and redistributing it towards more side-scattering angles (i.e., the angle at which the ray is deflected), resulting in lower asymmetry parameter values, relative to their pristine counterparts. Distortion

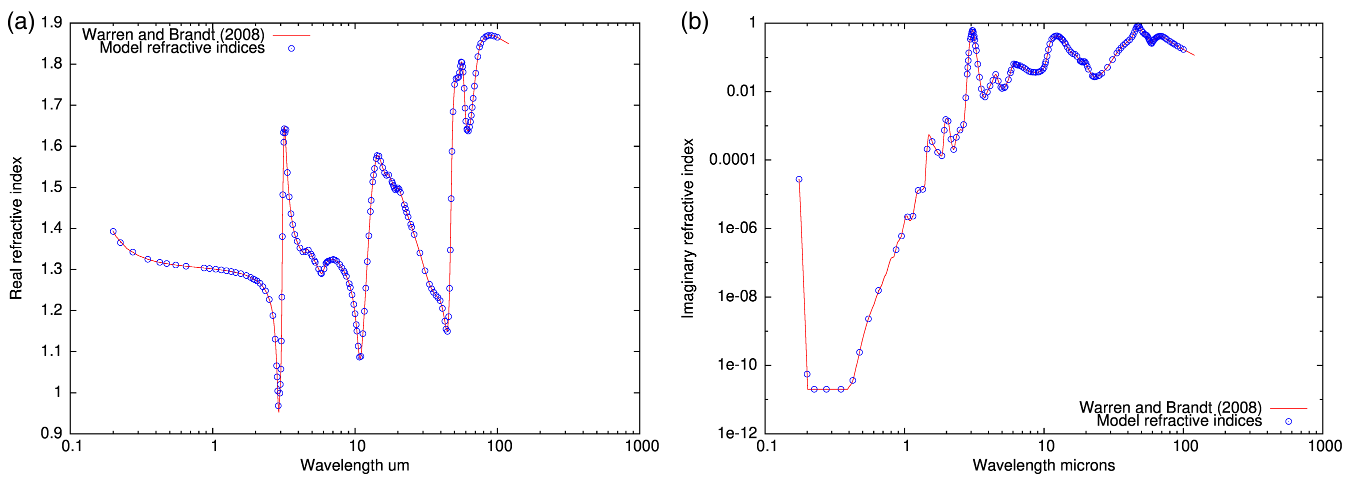

FIGURE 3 (a) Real and (b) imaginary refractive index of solid ice compiled by Warren and Brandt (2008) as a function of wavelength, where the full line represents the experimental values, and the open circles represent the 170 wavelengths at which the single-scattering properties were calculated. The key to the figure is shown at the top left and bottom right of the figure, respectively. [Colour figure can be viewed at wileyonlinelibrary.com] is a large-scale geometrical method that is supposed to represent micro-scale surface roughness and ice crystal irregularity. The degree of distortion is defined as $\theta_t / 90°$ and can take values between 0 (pristine) and 1. In this paper, as explained in Baran and Labonnote (2007), we apply a distortion value of 0.4 plus spherical air bubble inclusions to all six elements of the ensemble model. The spherical air bubble inclusions are set to a mean free path length of 200 μm throughout the model. The distortion value of 0.4 was chosen because this was found to best fit POLDER-2 (POLarization and Directionality of the Earth's Reflectances, see Buriez *et al.*, 2005) measurements of the spherical albedo and linearly polarised reflectance (Baran & Labonnote, 2006). For the distortion value of 0.4 plus spherical air bubble inclusions, the modifications made to the Macke *et al.* (1996) ray-tracing code by Shcherbakov *et al.* (2006) has been used. Because the random numbers representing θ_t were found by Shcherbakov *et al.* (2006) to be best represented by Weibull statistics rather than a uniform probability density function, the Weibull statistics better fitted their cloud chamber visible angular scattering measurements of the phase function.

At wavelengths greater than 5.0 μm, the total optical properties were calculated using the method of Baran (2003). In this method, the total optical properties are calculated using the T-matrix method (Mishchenko & Travis, 1998) by applying the aggregate electromagnetic scattering approximation developed by Baran (2003). It was shown by Baran (2003) that at wavelengths in the terrestrial window region, finite-difference time-domain calculations of the hexagonal ice aggregate (Yang & Liou, 1998) total optical properties could be calculated to well within 4% of the exact solutions using the approximation. This level of accuracy was achieved by approximating the aggregate using an ensemble of equal volume-to-area ratio circular cylinders of varying aspect ratios. This same electromagnetic approximation and ice model was used by Baran and Francis (2004) to simulate ARIES measurements to within ±1 K, between the wavelengths of 3.4 and 16.0 μm, obtained above semi-transparent cirrus off the northeast coast of Scotland during October 2000.

In the next section, the CASIM PSDs will be defined and described. These PSDs will be utilised to integrate over the single-scattering properties to determine the bulk optical properties using Equations (1)–(4).

3 | THE CASIM PSDS

The CASIM PSDs are represented by the generalised gamma distribution (Field *et al.*, 2023), and this same form of the PSD is used to generate the ensemble model bulk ice optical properties. The form of the generalised gamma distribution is described by the following equation:

$$N_{\mathrm{i,s}}(D) = n_{\mathrm{i,s}} \frac{\lambda_{\mathrm{i,s}}^{1+\mu_{\mathrm{i,s}}}}{\Gamma\left(1+\mu_{\mathrm{i,s}}\right)} D^{\mu_{\mathrm{i,s}}} \mathrm{e}^{-\lambda_{\mathrm{i,s}} D} \tag{5}$$

where $N_{\mathrm{i,s}}(D)$ is the number concentration of ice and snow particles of maximum size D, denoted by the subscripts i and s, respectively; D is in units of m. The parameters $n_{\mathrm{i,s}}$, $\lambda_{\mathrm{i,s}}$, and $\mu_{\mathrm{i,s}}$ are the total particle number concentrations of ice and snow in units of m^{-3}, and the slope and shape of the PSD, respectively; the slope, λ, is in units of m^{-1}.

The slope, $\lambda_{\mathrm{i,s}}$, follows directly from CASIM and is given by:

$$\lambda = \left(\left(\frac{\Gamma(1+\mu+P_1)}{\Gamma(1+\mu+P_2)} \right) \times \frac{m_2}{m_1} \right) \wedge \left(\frac{1}{P_1 - P_2} \right), \tag{6}$$

where the subscripts i and s have been omitted from all the terms for ease of reading. The terms m_1 and m_2 are the mass moment and the number moment, respectively; m_1 is related to the mass through the mass–dimension relation, $m_1 = \mathrm{mass}/C_x$, where C_x is the density of ice and snow. The units of mass are in kg per kg of cloudy air per unit volume, and the units of number are in per kg of cloudy air per unit volume. The terms P_1 and P_2 in Equation (6) represent the exponents of the moment equation, $M(P)$, of the PSD for mass and number, respectively. The moment equation is given by $M(P) = \int N(D) D^P dD$.

Ice particles in CASIM are assumed to be spatial, representative of bullet rosettes and polycrystals; so, $P_1 = 3.0$, $C_x = 104.7\ \mathrm{kg\,m^{-3}}$, and $P_2 = 0$ with $\mu = 2.5$. In the case of ice, with $P_1 = 3.0$, this setting assumes that the mass of ice is proportional to the third moment of the PSD. For snow, $P_1 = 2.0$ and $C_x = 0.026\ \mathrm{kg \cdot m^{-3}}$, consistent with the mass–dimension relationship proposed by Cotton *et al.* (2013) that represents the mass of aggregating ice particles. This relationship is currently used in the Met Office's Earth System Model ice microphysics scheme. This mass–dimension relationship aligns well with other independently derived mass–dimension power laws found in the literature. For example, Cotton *et al.* (2013) demonstrated strong agreement with the power law derived by Heymsfield *et al.* (2010). Additionally, Erfani and Mitchell (2016) found similar consistency in their analysis. More recently, McCusker *et al.* (2024) showed that the Cotton *et al.* (2013) power law is also in good agreement with the Brown and Francis (1995) relationship, provided the differences in size definitions are accounted for, by following Hogan *et al.* (2012). For snow, $P_2 = 0$, but $\mu = 2.0$. It should be noted here that the assumed prefactor of $104.7\ \mathrm{kg \cdot m^{-3}}$ for ice provides an effective density of about $200\ \mathrm{kg \cdot m^{-3}}$, which is different to the in-situ derived value of 700 kg·m^{-3} found by Cotton *et al.* (2013). However, Heymsfield *et al.* (2004) found in-situ densities ranging from approximately 100 to about 400 kg·m^{-3} in the cases they sampled. Therefore, there is still considerable latitude in the choice of the effective density value for ice.

To obtain the total number concentration, $N_{\mathrm{T}}(D)$, in each size bin of width dD, the two unimodal PSDs represented by Equation (5) are added together as follows:

$$N_{\mathrm{T}}(D) = N_{\mathrm{i}}(D) + N_{\mathrm{s}}(D), \tag{7}$$

To comply with the dimensions of Equation (5), the units of the mass of snow and ice, and the number from the CASIM outputs are converted into units of kg m^{-3} and m^{-3}, respectively, through the density of dry air (kg m^{-3}), which is obtained from the CASIM output. At cirrus-forming temperatures, the difference between the density of dry and moist air is negligible. Therefore, the choice of air density in this paper is inconsequential. In this paper, the considered size range varies from 1 to 28,121 μm, and the bin width for each PSD is set at 10 μm.

We compare the CASIM-derived PSDs with the PSDs assumed in the current ice optical parametrisation in the Met Office's Earth System Model (see Walters *et al.*, 2019) based on Baran *et al.* (2016), which is obtained from the moment estimation parametrisation of Field *et al.* (2007). This utilises the tropical normalisation of the PSD from Field *et al.* (2007) because this form of PSD agrees well with in-situ observations of moments and PSDs, as demonstrated by Furtado *et al.* (2015) and Baran *et al.* (2011), respectively. To generate the Field *et al.* (2007) PSDs, also known as F07, the total IWC and the environmental temperature are required as inputs to the parametrisation, as well as the assumed mass–dimension relation, which is the Cotton *et al.* (2013) relationship.

Figure 4 shows examples of the PSDs predicted by CASIM for various total in-cloud IWCs (that is, the sum of ice and snow IWCs), and in-cloud N_{T} values, at six environmental temperatures. To obtain the environmental temperature, T_{k}, from the model data, we used the temperature in Kelvin on model levels.

Figure 4 aims to illustrate the range in the CASIM PSDs for the given two-moment inputs. Additionally, the figure displays the equivalent F07 tropical, mid-latitude, and modified mid-latitude PSDs. The original F07 mid-latitude normalised PSD has recently been updated to account for current observations of the number concentrations of small ice crystals with sizes below 100 μm; refer to O'Shea *et al.* (2021) for further details. However, a brief description of the modified mid-latitude F07 PSD is given here. The F07 mid-latitude PSD was modified to account for recent observations indicating that many small ice crystals could be missized and hence incorrectly contribute to number concentration as well as potential shatter artefacts even after interarrival time filtering. The modification removes the smaller particle mode from the distribution and applies appropriate correction factors to the moment relationships to maintain consistency in the overall distribution. This results in fewer small particles (<100 μm) in the modified PSD compared to the original F07 mid-latitude parametrisation. Table 1 lists the various total in-cloud IWC, in-cloud N_{T}, and T_{k} values used for the Figure 4 comparisons, where in the figure T_{k} has been converted to °C.

In Figure 4, the CASIM PSDs can be just as broad as or even broader than the F07 PSDs. However, the shape of the CASIM PSDs can vary significantly depending on the two-moment inputs, although the ice and snow modes are present at all temperatures considered. It should be noted that the F07 PSD parametrisations are based on in-situ measurements that were obtained at temperatures no colder than approximately −65°C. The purpose of Figure 4 is to illustrate the variety of shapes of the CASIM PSDs and how these compare with the F07 tropical PSD that was used in the current ice optical parametrisation that is utilised in the GCM. This comparison is useful in explaining any differences observed in the radiation simulations between the new CASIM parametrisation and the current ice optical parametrisation. It should be noted that not all the CASIM PSDs will be like the ones presented in Figure 4, as the variation in the shapes of the CASIM PSDs can be very significant depending on the ice and snow inputs. The next section discusses the extraction of the two-moment inputs from the regional model runs.

4 | THE CASIM TWO-MOMENT DATA

The CASIM data used in this study are taken from the regional model runs centred on Darwin, Australia, and the UK, respectively. The data (from the regional model) used to construct the bulk ice optical property parametrisations are taken from the forecast runs after one day for both Darwin and the UK to allow some evolution of the cloudy fields. In the case of Darwin, the extracted data correspond to local midday and midnight for the period between 23 January and 17 March 2017. In the case of the UK, the data are extracted from local midday during the period between 6 December 2017 and 01 March 2018. The data are extracted from the summer and winter periods to cover as wide a range of the ice and snow moment values for the construction of the bulk ice optical property parametrisations. Both the UK and Darwin areas cover about 1000 km^2. The Darwin case contains deep tropical convection and warm-only cumulus. The UK area contains mid-latitude cloud. Both domains have land and

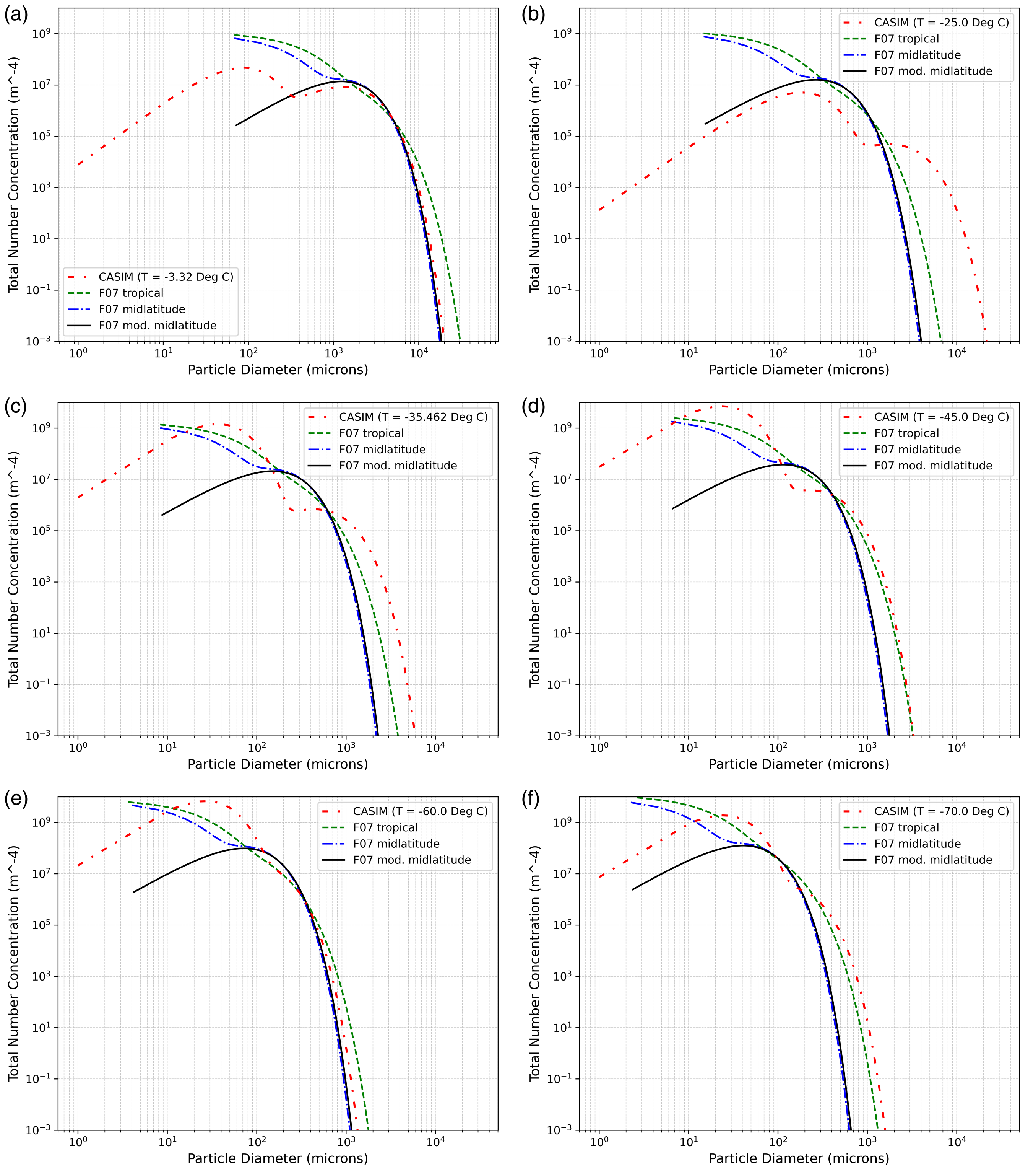

FIGURE 4 Shapes of some of the CASIM particle size distribution (PSDs) (represented by the dash-dot-dot lines) generated from the total in-cloud ice water content and N_T values given in Table 1. Also shown in the figure are the F07 tropical (dashed lines) and the modified mid-latitude (full black lines), and the mid-latitude (dash-dot lines) PSDs. The keys to each of the panels are shown in the figures. [Colour figure can be viewed at wileyonlinelibrary.com]

TABLE 1 Various arbitrarily selected T_c, in-cloud values of total IWC, and N_T are used to generate the CASIM and F07 PSDs shown in Figure 4

PSD	IWC ($g{\cdot}m^{-3}$)	N_T (cm^{-3})	T_c (°C)
1	2.78507	0.027	−3.0
2	0.04389	0.002	−25.0
3	0.14435	0.042	−35.0
4	0.00824	0.288	−45.0
5	0.00537	0.308	−60.0
6	0.00124	0.078	−70.0

Note: IWC, ice water content; PSD, particle size distribution.

ocean areas. These areas are the same as used in the paper by Bush *et al.* (2024). From the two regional models a subset of the total amount of ice and snow data was extracted.

This subset of data was extracted to ensure the data used in the bulk optical property parametrisation would be radiatively active, and that the in-cloud values were sensible when converted from their grid box-averaged values. To this end, the cloud fractions extracted were not less than 0.05, as values less than this would not likely be detected by space-based radiometric observations as suggested in the study by Wang and Zhao (2016). Here, the nondetection of the cloud fraction less than 0.05 by radiometric observations is taken as a proxy for whether the cloud is radiatively active. Further, total IWCs less than 0.002 $g{\cdot}m^{-3}$ were excluded from the subset of data, and total number concentrations less than 100 m^{-3} were also excluded from the analysis. This was because IWC values less than the above threshold would have very small column integrated amounts, and these clouds would not significantly interact with the radiation field. The total IWC threshold was set to 0.002 $g{\cdot}m^{-3}$ because this is the detectable limit of the in-situ IWC probe as found in the study by Abel *et al.* (2014). Likewise, in the case of the total number concentrations, the threshold limit of 100 m^{-3} was set because in-situ instruments used in the global study by Krämer *et al.* (2016) did not include number concentrations less than this.

The subset of data extracted from the Darwin and UK case studies using the above filters comprise local midday and midnight. From this data collection, the best distributions of ice and snow number values were selected, and these days were combined into a single dataset from the Darwin and UK data. The distribution of the ice and snow number and mass from this single dataset is shown in Figure 5a,b as bivariate histogram plots. The bar shown on the right side of Figure 5a,b represents the count of data points within each bin, with the scale ranging from single to thousands of occurrences. These visualisations clearly reveal the most common mass–number relationships in the dataset.

In Figure 5a, a broad distribution of ice crystals is evident with a high-density region showing a positive

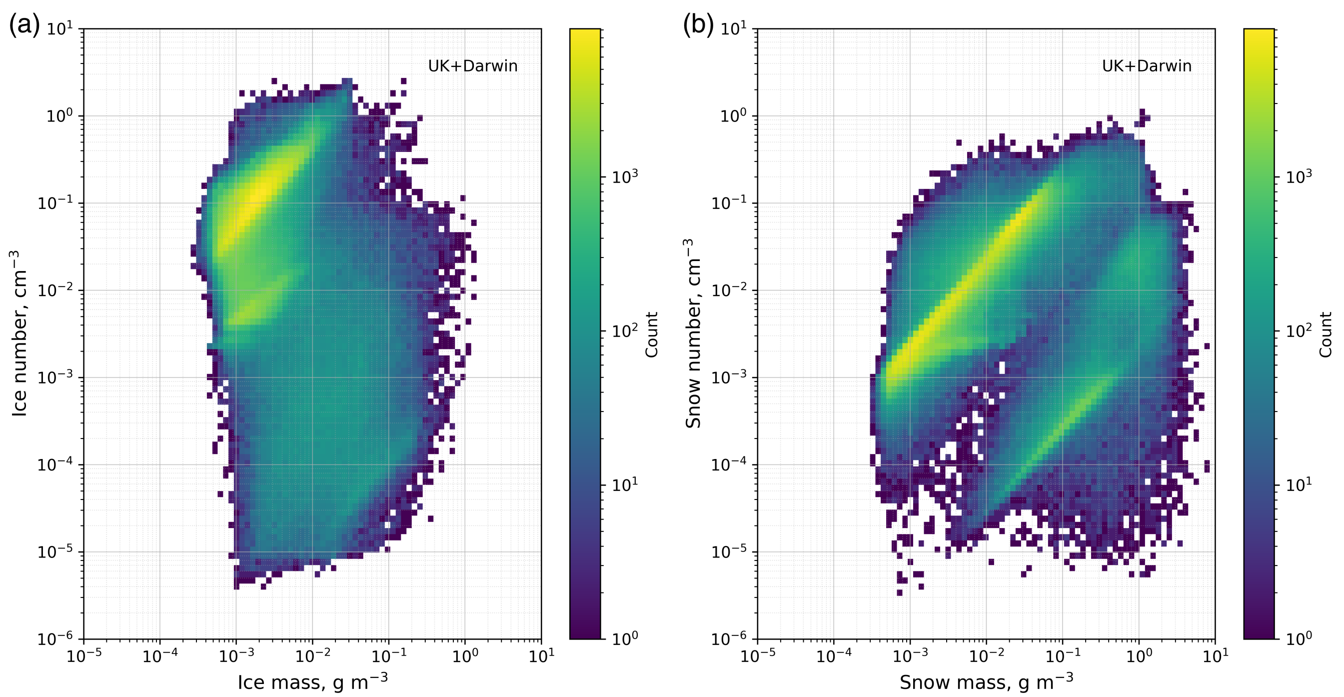

FIGURE 5 The combined regional model distributions of (a) in-cloud ice number and ice mass and (b) in-cloud snow number and snow mass for the two best days from the Darwin and UK data. The key is shown on the right side of each of the panels. [Colour figure can be viewed at wileyonlinelibrary.com]

correlation between ice number and mass. The densest region appears at moderate ice number and mass values. Figure 5b reveals a distinct pattern for snow particles, with two prominent high-density bands displaying different mass–number relationships. These diagonal structures likely represent different snow formation or growth processes occurring in the model simulations. The sparsely populated dots around the periphery of both distributions indicate infrequent combinations of number and mass values, effectively highlighting the boundaries of physically realistic parameter spaces in the model.

The complete data distributions for each of the locations for all days are not shown for the sake of brevity. From Figure 5, the ice and snow moments appear to be quite realistic distributions on which to base the ice optical parametrisation and are well distributed in the spaces of the moments. This probably helps to explain why the CASIM PSDs in Figure 4 compare favourably with the F07 PSDs, with the latter known to be representative of observed PSDs.

Figure 5 exhibits a total number of about 10^8 data points, which is too large to generate the PSDs and store the optical properties in SOCRATES. To reduce this number of points to a more manageable size, random sampling was performed to obtain a reduced dataset, resulting in 62,250 CASIM PSDs. To demonstrate that there was no bias introduced into the reduced dataset, Figure 6 presents a comparison of the frequency distributions of ice number concentration and ice water content in the unreduced and reduced datasets. It is evident from Figure 6 that there is no statistical difference between the probability density functions (PDFs) of the unreduced and reduced two-moment datasets. Therefore, randomly reducing the original dataset to a size that enables efficient computation of the bulk ice optical properties will not introduce any bias in the CASIM prognostic moments.

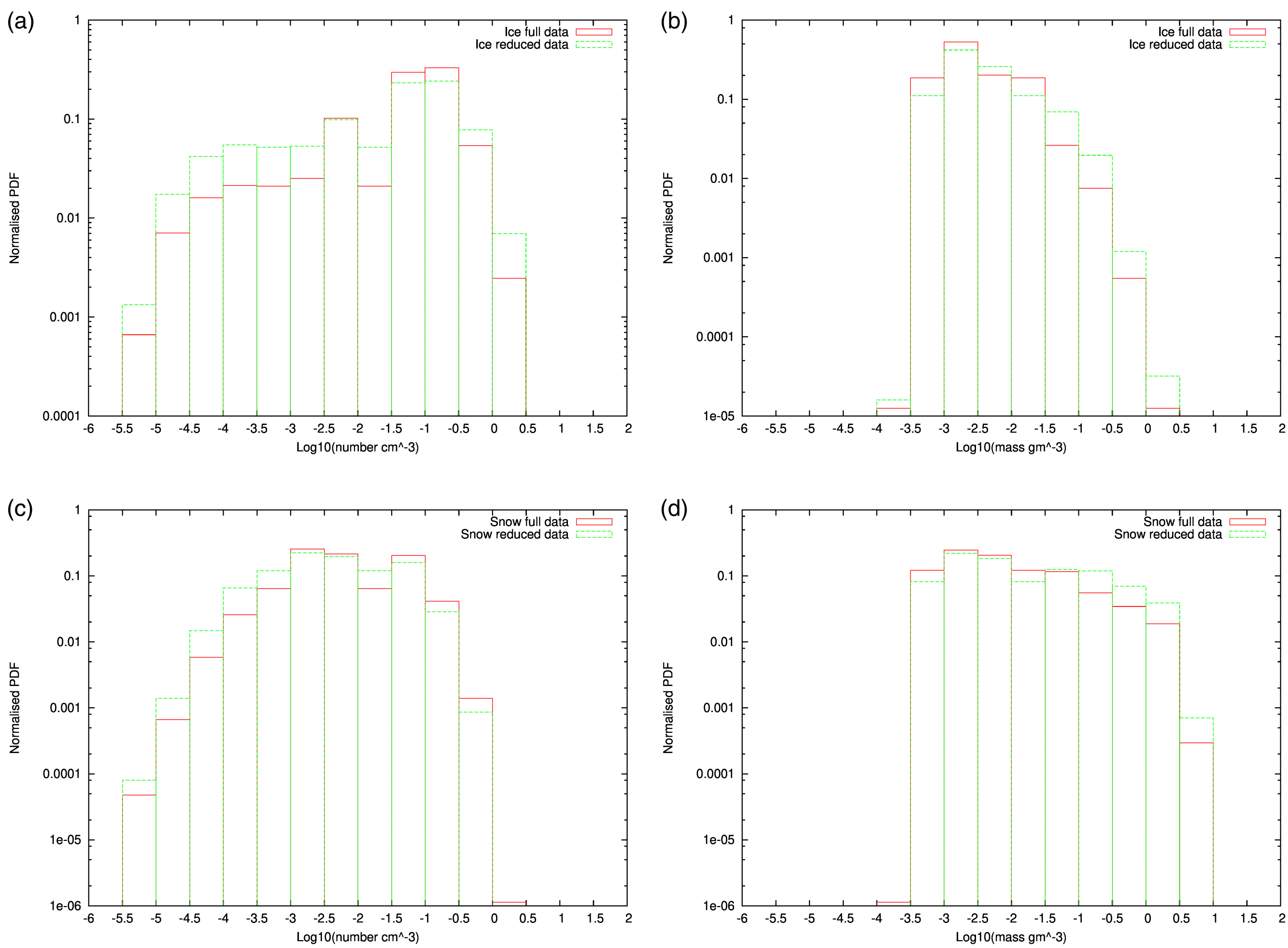

FIGURE 6 A comparison of the normalised probability density functions (PDFs) of the unreduced data, shown as the full line histograms, with the reduced data, shown as the dashed histograms for (a) $\log_{10}$(ice number), (b) $\log_{10}$(ice mass), (c) $\log_{10}$(snow number), and (d) $\log_{10}$(snow mass). The keys to each of the panels are shown at the top right of the figure. [Colour figure can be viewed at wileyonlinelibrary.com]

5 | PARAMETRISATION OF THE CASIM BULK ICE OPTICAL PROPERTIES

The bulk optical properties of the ensemble model have been calculated using the distribution of the members of the ensemble as described in Section 2. The bulk optical properties have been calculated using the CASIM inputs (i.e., in-cloud ice and in-cloud snow mass, and in-cloud ice number and in-cloud snow number) described in Sections 3 and 4 to obtain the CASIM-predicted generalised gamma function PSDs presented in Section 3. These have no dependence on in-cloud temperature, and only the in-cloud total mass and total number, predicted by CASIM and they are in units of $\mathrm{kg\cdot kg^{-1}}$ and $\mathrm{number\cdot kg^{-1}}$ respectively, and are related to the bulk ice optical properties. This eliminates the need for unit conversions within the model. The 62,250 CASIM PSDs being used to compute the bulk ice optical properties according to Equations (1)–(4), these being the bulk extinction and scattering coefficients, C_{ext}, and C_{sca}, respectively, the single-scattering albedo, ω_0, and the asymmetry parameter, g.

Here, a database has been generated that consists of 62,250 values of total in-cloud ice mass mixing ratio and number. These values are followed by 170 wavelengths between 0.175 and 100 μm, and at each wavelength, the bulk scattering and absorption coefficients and the asymmetry parameter are provided. However, the total size of the database is 667 MB; this is too large a size for implementation within the SOCRATES spectral files, so it had to be reduced to a more manageable size. To achieve this, a new routine within SOCRATES called reduce_casim_ice was provided, which repeatedly bisects the data into parts containing equal numbers of data points in order of mass mixing ratio and mean particle mass (i.e., the ratio between the total in-cloud ice mass and the total in-cloud number). It then outputs a reduced database of 1026 blocks of averaged properties to reduce the size of the database down to 14 MB in a format that is readable by the existing scatter_average routine within SOCRATES.

It was found that the optical properties are well described as a function of the mean ice crystal mass, which allows the traditional fitting methods to be used. Here, we apply the technique using Padé approximants (i.e., see the form of these in Equation 9 below) to fit the mass extinction coefficient, and the co-albedo and the asymmetry parameter from the database as a function of mass-equivalent spherical radius (effectively, a constant times the cube root of the mean ice crystal mass) having the same mass and solid density as a non-spherical ice crystal. This is the same flexible fitting technique used for water cloud droplets, but it has not been used for ice crystals before. Combining the two prognostic variables to derive the mean ice crystal mass per particle reduces the number of dimensions that are directly input to the radiation scheme. By utilising the same methodology of fitting the bulk ice optics that was used for water droplets, we treat water and ice consistently within the radiation scheme. To achieve this consistency, we must rewrite the existing Padé approximants in terms of the mass-equivalent spherical radius, $r_{\overline{\mathrm{m}}}$, for the mean ice crystal mass per particle rather than the effective radius, where $r_{\overline{\mathrm{m}}}$ is defined by:

$$r_{\overline{\mathrm{m}}} = \left(\frac{3I\rho_{\mathrm{air}}}{4\pi N \rho_{\mathrm{ice}}} \right)^{\frac{1}{3}}, \tag{8}$$

where I is the ice mass mixing ratio, ρ_{air} is the density of dry air, ρ_{ice} is the density of solid ice assumed to have the value of $917\ \mathrm{kg\cdot m^{-3}}$, and N is the total number concentration in units of $\mathrm{m^{-3}}$.

The Padé approximants utilised here are given by the following set of relations (Manners *et al.* 2023):

$$k_{\mathrm{ext}} = I\frac{l_1 + l_2 r_{\overline{\mathrm{m}}} + l_3 r_{\overline{\mathrm{m}}}^2}{1 + l_4 r_{\overline{\mathrm{m}}} + l_5 r_{\overline{\mathrm{m}}}^2 + l_6 r_{\overline{\mathrm{m}}}^3},$$

$$k_{\mathrm{sca}} = k_{\mathrm{ext}}\left(1 - \frac{l_7 + l_8 r_{\overline{\mathrm{m}}} + l_9 r_{\overline{\mathrm{m}}}^2}{1 + l_{10} r_{\overline{\mathrm{m}}} + l_{11} r_{\overline{\mathrm{m}}}^2}\right),$$

$$g = \frac{l_{12} + l_{13} r_{\overline{\mathrm{m}}} + l_{14} r_{\overline{\mathrm{m}}}^2}{1 + l_{15} r_{\overline{\mathrm{m}}} + l_{16} r_{\overline{\mathrm{m}}}^2}, \tag{9}$$

where the k_{ext} and k_{sca} terms are the mass extinction and scattering coefficients, respectively, defined as $C_{\mathrm{ext,sca}}/I\rho_{\mathrm{air}}$. The lth coefficients in Equation (9) for k_{ext} and k_{sca} are chosen such that the well-known inverse relationship between the mass coefficients and $r_{\overline{\mathrm{m}}}$ is replicated as $r_{\overline{\mathrm{m}}}$ becomes larger. The single-scattering albedo and co-albedo are found simply from Equation (3). In Equation (9), the total ice optical properties are directly linked to $r_{\overline{\mathrm{m}}}$ rather than r_{e}. This choice is driven by the fact that $r_{\overline{\mathrm{m}}}$ is derived directly from model prognostic variables – mass mixing ratio (I) and number (N) – ensuring a physically consistent representation of ice optical properties within the model. In contrast, r_{e} is fundamentally area-weighted, and since area is not a prognostic variable in most models, it must be parametrised using empirical relationships. This reliance on additional assumptions introduces uncertainties that we aim to avoid, as well as the other limitations highlighted in the introduction to this paper.

The spectral averaging techniques used in this paper are based on the study of Hogan and Matricardi (2022), who found that, following Edwards and Slingo (1996), using 'thin' and 'thick' spectral averaging is more accurate in replicating cloudy irradiances than using other techniques. For optically thin clouds or cirrus with low optical depths, linear averaging is appropriate to compute the optical properties. In this case, the mass extinction coefficient, the co-albedo, and the asymmetry parameter are spectrally averaged (weighted by the solar or Planck irradiance) as has been done previously. This is called 'thin' averaging because such a linear weighting of the optical properties is only exact in the limit of optically thin clouds. However, in the model and observations, most clouds are not optically thin. In this case, it is more appropriate to use a weighting that is better for the radiative properties of optically thick clouds. For optically thick clouds or 'thick' spectral averaging, the reflection coefficient of an infinite optically thick cloud is calculated, and weighted, and the total extinction is weighted rather than the individual coefficients. Hogan and Matricardi (2022) concluded that 'thick' spectral averaging is the best choice for most cases of calculating cloudy irradiances. In previous papers, the recommendations of Edwards and Slingo (1996) were followed, which were that 'thin' and 'thick' spectral averaging should be applied to cirrus and water clouds, respectively. Here, we trial 'thick' and 'thin' spectral averaging.

The fits obtained using the Padé approximants with the standard six-band short-wave and nine-band long-wave spectral files are found to be very good for all the wavelength ranges for these spectral files. The bands used, as presented by Walters *et al.* (2019), are provided in Tables 2 and 3. An example of the Padé-approximant fitting to spectral band 3 is presented in Figure 7. All other bands are fitted equally well, and all bands can be found in the Supporting Information, presented in Figures S1–S5. It should be noted that in Figure S1, the fit to the co-albedo for bands 1 and 2 appears poor. This is because the co-albedo for these two bands is very close to zero, indicating effectively no absorption. In obtaining Figure 7, the bulk ice optical properties, in-cloud ice mass mixing ratios, and ice number concentrations were initially computed using 62,250 distinct PSDs derived from CASIM. To make subsequent analysis computationally tractable, this extensive dataset was reduced by grouping PSDs into 1026 bins. Importantly, these bins were not formed by simply averaging properties within equal intervals of mean particle mass. Instead, the bins were generated by repeatedly bisecting the entire dataset into equal numbers of PSDs in a two-dimensional parameter space, defined by the mass mixing ratio and the mean particle mass per particle.

This deliberate approach was chosen explicitly to preserve any potential dependencies of optical properties on both these microphysical parameters. Upon inspection,

TABLE 2 Spectral bands for the short-wave band. The table is adapted from Walters *et al.* (2019)

Short-wave band	Wavelength (μm)
1	0.200–0.320
2	0.320–0.505
3	0.505–0.690
4	0.690–1.190
5	1.190–2.380
6	2.380–10.00

TABLE 3 Spectral bands for the long-wave band. The table is adapted from Walters *et al.* (2019)

Long-wave band	Wavelength (μm)
1	25.0–10,000
2	18.18–25.0
3	12.5–13.33 & 16.95–18.18
4	13.33–16.95
5	8.33–8.93 & 10.10–12.50
6	8.93–10.10
7	7.52–8.33
8	6.67–7.52
9	3.34–6.67

however, it became apparent that the bulk optical properties exhibited minimal sensitivity to variations in mass mixing ratio. Consequently, the data points from these irregular bins collapsed predominantly onto a monotonic function of mean particle mass per ice crystal. This feature justified the use of mean ice crystal mass – and specifically the mass-equivalent spherical radius – as the primary variable for fitting the Padé approximants.

Thus, although the relationship between mass-equivalent spherical radius and bulk optical properties appears clearly defined in Figure 7 due to binning, the initial binning strategy itself did not inherently impose this relationship. Rather, it emerged naturally from the data. This is further demonstrated in the Supporting Information (Figures S6–S8), which shows the scaled mass extinction coefficient, mass scattering coefficient, and asymmetry parameter derived from all 62,250 PSDs for Band 3 of the long-wave Edwards–Slingo bands. The same scaling approach described in the caption of Figure 7 has been applied. These supplementary figures confirm that the bulk optical properties collapse onto tight, well-defined curves as a function of r_{m}, with minimal dispersion, and can be accurately captured using Padé approximants of the same rational polynomial form as

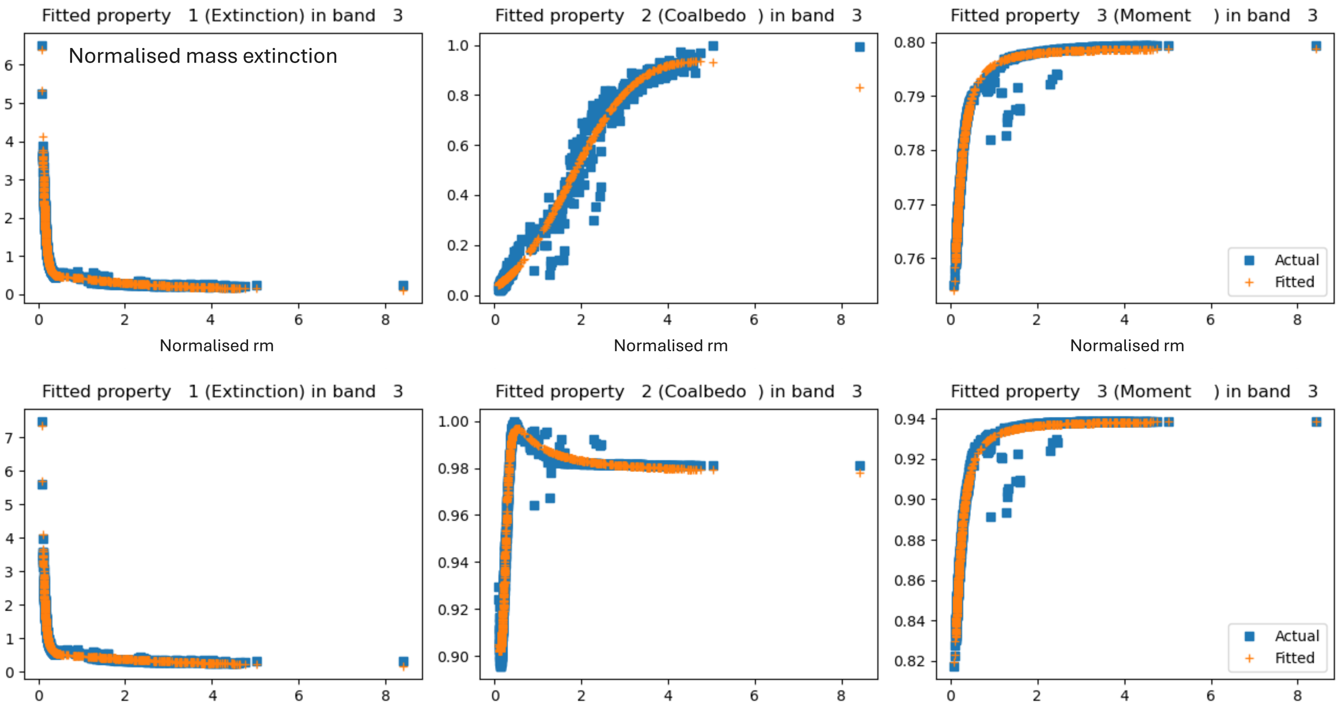

FIGURE 7 Fitting of the Padé approximants (plus signs) to the binned data (squares) for band 3 of the short wave in the top panel and long wave in the bottom panel. The x-axis represents the mass-equivalent spherical radius (r_m) scaled by dividing by the mean value over all data, while the y-axis represents different scaled optical properties: Mass extinction coefficient divided by its mean value over all data (first left panel), co-albedo divided by its maximum value over all data (centre panel), and the asymmetry parameter (dimensionless) is shown in the right-most panel. [Colour figure can be viewed at wileyonlinelibrary.com]

Equation (9). Comparisons between the Padé fits and the original data (Figures S9–S11) show excellent one-to-one agreement, confirming the reliability of the fits across the full PSD ensemble.

Figure 7 serves as an example of how well the Padé approximants fitted the binned data. Specifically, the figure showcases how the approximants for band 3 (from Tables 2 and 3) replicated the binned data. As can be seen from the figure, the fits accurately describe the binned data. In Figure 7, there are 1026 plotted points so it can be seen on the plots that the number of outliers is small. However, it should be noted that the binned data are somewhat noisy; this is likely due to stronger bimodality in the CASIM PSDs. However, the number of noisy points is small, and thus, they will not detract from the accuracy of the Padé fits.

The accuracies of the Padé fits for each band, as shown in Tables 2 and 3, were assessed using the coefficient of determination (r^2) and the root mean square (rms). On average, the r^2 values across all six short-wave bands for the mass extinction coefficient and asymmetry parameter were 99.72% and 98.96%, respectively. For the non-absorbing bands (i.e., bands 1 and 2), the error in the co-albedo was evaluated using the rms, which was found to be less than 10^{-6}. This is because the co-albedo values at these non-absorbing bands are extremely small, making r^2 an unsuitable metric for such cases. For the four absorbing short-wave bands, the average r^2 value for the co-albedo was 97.62%.

For the long-wave bands, the average r^2 values across all nine bands for the mass extinction coefficient, co-albedo, and asymmetry parameter were 99.65%, 96.99%, and 98.99%, respectively. These results demonstrate that the Padé fits provide sufficiently accurate parametrisations for the purposes of this study.

The next section will describe and discuss the impact of using the coupled consistent parametrisations in the regional model.

6 | THE IMPACT OF THE COUPLED CONSISTENT PARAMETRISATIONS ON THE RADIATION FIELDS IN THE REGIONAL MODEL

The simulations presented in this section utilised an existing Darwin case study that had been used to evaluate various CASIM configurations and the operational regional model against the CERES (Clouds and Earth's Radiant Energy System, see Loeb *et al.*, 2016 for further information about CERES) short- and long-wave measurements. In this comparison, the outgoing short- and long-wave irradiances at the TOA were compared to the CERES 1° hourly product (i.e., 10.5067/TERRA+AQUA/CERES/SYN1DEG-1HOUR_L3.004A). The results of the comparisons are presented in Figure 8, where histograms for all-sky situations were produced by presenting approximately 60 days of $T+27$ output from 0Z (about local midday) as a histogram, with the days being contiguous. Results using the Met Office's next operational regional atmosphere–land model called ral3.1 with the current ice optical parametrisation are also shown in Figure 8.

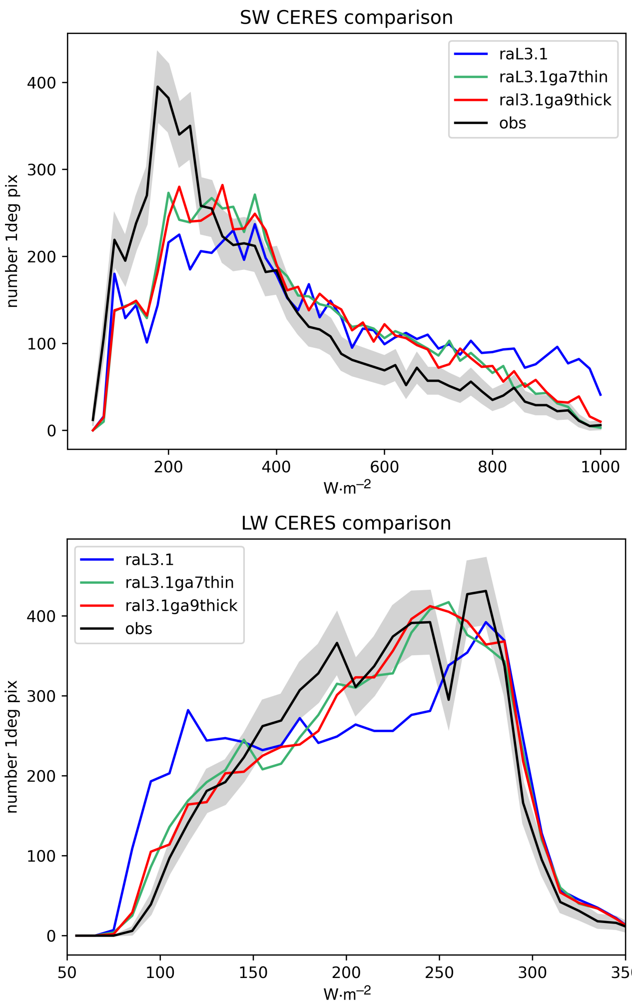

FIGURE 8 The comparison between CERES observations for Darwin and ral3.1 using different spectral averaging techniques is shown in both the short-wave (top panel) and long-wave bands (bottom panel). The CERES observations are depicted as a solid black line with a two-times Poisson uncertainty envelope, while the 'thin' and 'thick' spectral averaging techniques are described in the key in each panel. Note, in terms of radiation, differences between ga7 and ga9 are not significant here and so have no impact on the radiation calculations. [Colour figure can be viewed at wileyonlinelibrary.com]

The short-wave results shown in the top panel of Figure 8 demonstrate that the new CASIM-coupled consistent parametrisation (shown as the full green and red lines in the figure) replicates the high-irradiance end of the CERES short-wave observations (shown as the full black line in the figure) better than the single-moment current ice optical parametrisation (shown as the full blue line in the figure) described in Baran *et al.* (2016). For irradiances between 800 and 1000 $\mathrm{W \cdot m^{-2}}$, the spectral averaging results using the consistent two-moment parametrisation achieved an Agreement Index of 0.74 (Willmott, 1981), indicating generally good agreement with the observations. While the parametrisation tends to overestimate pixel counts relative to the observations, this overestimation is significantly reduced compared to the single-moment parametrisation. Indeed, the single-moment parametrisation significantly overestimates the number of pixels relative to the observations, resulting in an Agreement Index of only 0.32, indicating poor agreement. In contrast, the consistent two-moment parametrisation improves this considerably, thereby providing a more accurate representation of the observed distribution at the high-irradiance end. The long-wave results, shown in the bottom panel of Figure 8, demonstrate excellent agreement between the CERES measurements and the new CASIM-consistent coupled parametrisation simulations. In particular, at the low-irradiance end of the long-wave range ($<150\,\mathrm{W \cdot m^{-2}}$), the spectral averaging results achieved an Agreement Index of 0.97, capturing the observed trends with minimal deviations. However, when using ral3.1 with the single-moment Baran *et al.* (2016) ice optical parametrisation, the Agreement Index found for the single-moment parametrisation was 0.91 for irradiances $<150\,\mathrm{W \cdot m^{-2}}$. However, visual inspection of the bottom panel of Figure 8 reveals clear discrepancies in the distribution shape relative to observations. In particular, the single-moment parametrisation overestimates the number of low-irradiance pixels and exhibits a less realistic gradient, which is not fully captured by the Agreement Index metric. In contrast, the two-moment scheme follows the observed distribution closely, both in magnitude and shape, yielding a higher Agreement Index of 0.97 and qualitatively superior agreement.

It should be noted from Figure 8 that the differences between the 'thin' and 'thick' spectral averaging techniques are small. Therefore, results will only be presented for the case of 'thick' spectral averaging, following the recommendation of Hogan and Matricardi (2022).

The CERES short- and long-wave irradiance measurements provide insight into cloud optical depth properties. In the short-wave histogram, higher TOA irradiances

(800–1000 W·m^{-2}) typically indicate greater cloud reflectivity associated with optically thicker clouds or higher cloud fractions, while in the long-wave histogram, lower irradiances (<150 W·m^{-2}) generally correspond to higher, colder cloud tops with greater optical depth that trap outgoing thermal radiation more effectively.

Figure 9 shows the radiation results obtained around the UK using 'thick' spectral averaging. Again, the CERES 1° hourly product is utilised, where histograms for all-sky situations were produced by presenting approximately 40 days of $T+27$ output from 12Z (about local midday) as a histogram, with the 40 days being contiguous. Shown in Figure 9 are comparisons between the CERES observations and the current Met Office operational regional model called ra2m with the Baran *et al.* (2016) single-moment parametrisation, shown as the solid blue line, CASIM with the coupled consistent parametrisation is shown as the solid green line, and the same but with the Baran *et al.* (2016) parametrisation is shown as the solid red line.

We also compare the effect of the new parametrisation with the results using Baran *et al.* (2016). The results presented in Figure 9 show that in the short wave band (left panel), the CASIM coupled consistent ice optical parametrization's agreement with the CERES measurements is better than the ice optics in ra2m, which uses Baran *et al.* (2016), and the CASIM ice optical parametrization also from Baran *et al.* (2016). The coupled consistent CASIM optical parametrisation captures the peak of the CERES short-wave measurements and is in general within the Poisson uncertainty over the range of the histogram. In the short-wave region, the two-moment parametrisation (casim3p1_rad) achieves an Agreement Index of 0.95, indicating strong agreement with the observed distribution over the range of the histogram. In contrast, the current operational model (ra2m) scores lower, with an Agreement Index of 0.87. These results reinforce the improved fidelity of the two-moment parametrisation in representing observed short-wave radiative distributions.

However, in the long-wave band (right panel), we see that the coupled consistent CASIM optical parametrisation is too transmissive and not transmissive enough at the higher and lower irradiance end of the CERES measurements, respectively. In the long-wave irradiance range of 140–260 W·m^{-2}, which encompasses the peak of the observed outgoing long-wave radiation distribution, the single-moment parametrisation (ra2m) outperforms the two-moment scheme (casim3p1_rad) in terms of agreement with observations. Specifically, the Agreement Index for the single-moment parametrisation is 0.74, compared to 0.60 for the two-moment parametrisation. This difference is consistent with the overestimation of emission evident in Figure 9, where the two-moment scheme predicts a greater number of high-irradiance pixels near the distribution peak. The reason for this long-wave result could be owing to the clouds not being at the correct altitude or error in the cloud fractions, and/or the PSDs being too narrow in this region. The single-moment Baran *et al.* (2016) parametrisations more closely follow the PDF of the CERES measurements in the long-wave, but this is likely due to error cancellation.

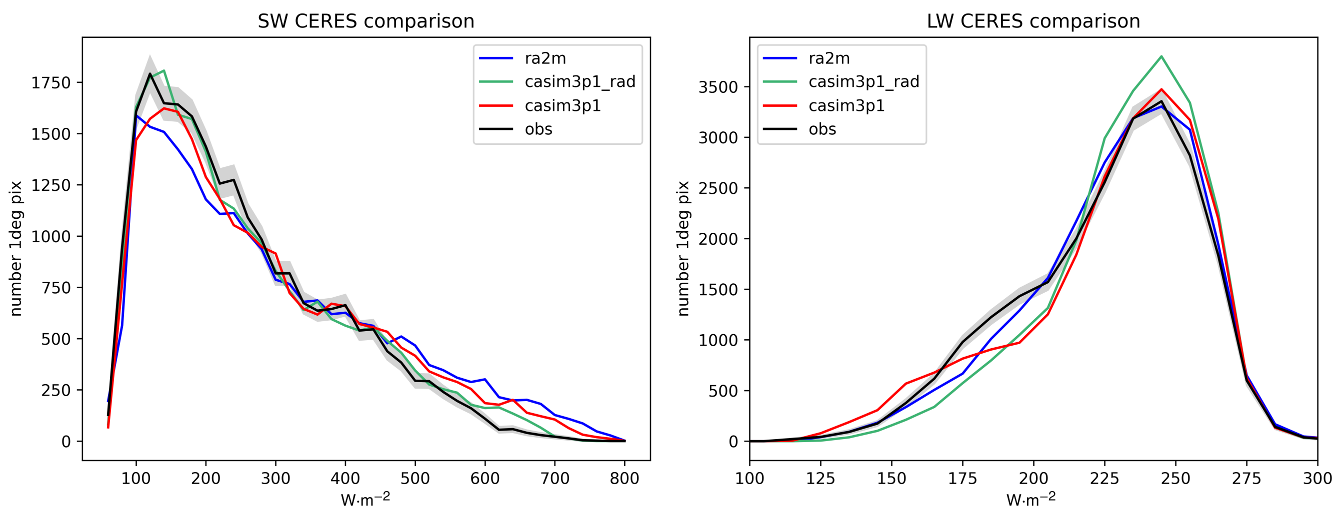

FIGURE 9 The comparison between CERES observations and ra2m (blue solid line) using 'thick' spectral averaging is shown in both the short-wave (left panel) and long-wave bands (right panel). The CERES observations are depicted as a solid black line with a two-times Poisson uncertainty envelope, while the new coupled consistent optical parametrisation (casim3p1_rad) and the Baran *et al.* (2016) single-moment ice optical parametrisation (casim3p1) are described in the key in each panel. [Colour figure can be viewed at wileyonlinelibrary.com]

The overall comparison between the CERES measurements and the new coupled consistent CASIM parametrisation simulations is improved over the single-moment radiation, with particularly good agreement at the low-irradiance end of the long-wave results, the higher end of the short-wave results, and in the case of around the UK the agreement with the CERES measurements is generally good in the short-wave band. Clearly, the overall results suggest that by consistently coupling the ice optics to two-moment microphysics the radiation fields are better simulated when comparisons are made with space-based measurements. Only with such a consistency can we hope to reduce the uncertainties in the cirrus radiative effect.

7 | DISCUSSION AND CONCLUSIONS

The work presented in this paper is based on the ensemble model of cirrus ice crystals, which generated a fully consistent two-moment look-up table of the bulk ice optical properties across 170 wavelengths, ranging from 0.175 to 100 μm. This look-up table was used to develop a new coupled consistent parametrisation of the bulk ice optics based on the two-moment input from CASIM. The two-moment input to the parametrisation includes the total in-cloud ice mass mixing ratio and number, which are combined to obtain the mean ice crystal mass per ice crystal.

From the mean ice crystal mass per ice crystal, the mass-equivalent spherical radius is derived, which has the same mass and solid density as the nonspherical particle. It has been shown that expressing the mean ice crystal mass per ice crystal in terms of the mass-equivalent spherical radius accurately describes the binned bulk ice optical properties as a function of size. This approach enables the use of existing Padé approximant techniques to fit the binned bulk ice optical properties as a function of mass-equivalent spherical radius accurately. This fitting technique, previously used for water droplet parametrisations, has been applied here for the first time for ice crystal optical property parametrisations. The main difference between water cloud and ice crystal bulk optical parametrisations is that the effective radius has been replaced by the mass-equivalent spherical radius for ice. The accuracy of fitting the binned bulk ice optical properties for the standard six-band short-wave and nine-band long-wave spectral files using the Padé approximants was found to be sufficiently accurate for the purposes of this paper. The paper also explored the use of 'thin' and 'thick' spectral averaging techniques for the ice optics. The findings of this paper can be summarised as follows:

1. The two-moment CASIM PSDs were compared with the F07 moment estimations in Figure 4 for the mid-latitude and tropical normalisations of the PSD over a wide range of temperatures and mass. The results showed that the new CASIM PSDs compared favourably with F07, which is well-known for representing cirrus and ice cloud PSDs.
2. The Darwin all-sky case study, conducted over 40 days, showed that the new coupled consistent two-moment ice optical parametrisation improved agreement with the CERES short-wave measurements, particularly at the high-irradiance end. The new CASIM parametrisation was found to be in better agreement with the CERES measurements than the single-moment Baran *et al.* (2016) ice optical parametrisation. This conclusion was also true for the long-wave measurements.
3. The 'thin' and 'thick' spectral averaging techniques were evaluated in the Darwin case study, and no significant differences were found. As a result, regional model simulations around the UK were performed using the 'thick' spectral averaging technique, following the recommendation of Hogan and Matricardi (2022).
4. The results around the UK using 'thick' averaging showed that the simulation of the CERES short-wave measurements using the new coupled consistent ice optical parametrisation was in remarkably good agreement with those measurements. However, in the long-wave band, the new parametrisation was somewhat too transmissive relative to the CERES measurements. This discrepancy could be due to clouds not being at the correct altitude, errors in cloud fractions, or the PSDs being too narrow in this region.

In this paper, we have demonstrated that a consistent coupling between the two CASIM prognostic moments, namely mass and number, and the ice optical properties have a very beneficial impact on radiation simulations in a regional weather model across different parts of the world. This achievement is particularly significant for regions known to be problematic for weather models, such as around Darwin, Australia, due to the deep convective clouds and semi-transparent cirrus that entrain off the convective clouds. Moreover, the consistency presented here no longer precludes the important analogous ice Twomey effect from occurring within CASIM, whether positive or negative, in the same way as it is present for liquid clouds. At the Met Office we can now incorporate aerosol within CASIM, but the sensitivity of radiation to the aerosol–ice coupling is left to later work. Only through such a consistent coupling between microphysics and radiation using two-moment rather than single-moment microphysics can we hope to more realistically simulate the cirrus radiation effects in weather and climate models and reduce their uncertainties. Additionally, such a consistent coupling should produce more interesting radiative feedbacks that are precluded in single-moment schemes.

DATA AVAILABILITY STATEMENT

The data used in this study are available from the Met Office's Science Repository upon request by accessing the SOCRATES website, located here: SOCRATES. The full 62,250 bulk optical property database is also available on request from Dr Anthony J. Baran (anthony.baran@metoffice.gov.uk).

ORCID

Anthony J. Baran https://orcid.org/0000-0001-5664-1411
James Manners https://orcid.org/0000-0003-4402-6811
Paul R. Field https://orcid.org/0000-0001-8528-0088
Kalli Furtado https://orcid.org/0000-0002-5166-112X

REFERENCES

Abel, S.J., Cotton, R.J., Barrett, P.A. & Vance, A.K. (2014) A comparison of ice water content measurement techniques on the FAAM BAe-146 aircraft. *Atmospheric Measurement Techniques*, 7, 3007–3022. Available from: https://doi.org/10.5194/amt-7-3007-2014

Bae, S.Y., Hong, S.-Y. & Lim, K.-S.S. (2016) Coupling WRF double-moment 6-class microphysics schemes to RRTMG radiation scheme in weather research forecasting model. *Advances in Meteorology*, 2016, 5070154. Available from: https://doi.org/10.1155/2016/5070154

Bailey, M.P. & Hallett, J. (2009) A comprehensive habit diagram for atmospheric ice crystals: confirmation from the laboratory, AIRS II, and other field studies. *Journal of the Atmospheric Sciences*, 66, 2888–2899.

Baran, A.J. (2003) Simulation of infrared scattering from ice aggregates by use of a size-shape distribution of circular ice cylinders. *Applied Optics*, 42, 2811–2818.

Baran, A.J. (2009) A review of the light scattering properties of cirrus. *Journal of Quantitative Spectroscopy and Radiative Transfer*, 110(14–16), 1239–1260.

Baran, A.J. (2012) From the single-scattering properties of ice crystals to climate prediction: a way forward. *Atmospheric Research*, 112, 45–69. Available from: https://doi.org/10.1016/j.atmosres.2012.04.010

Baran, A.J., Connolly, P.J., Heymsfield, A.J. & Bansemer, A. (2011) Using in situ estimates of ice water content, volume extinction coefficient, and the total solar optical depth obtained during the tropical ACTIVE campaign to test an ensemble model of cirrus ice crystals. *Quarterly Journal of the Royal Meteorological Society*, 137, 199–218. Available from: https://doi.org/10.1002/qj.731

Baran, A.J., Cotton, R., Furtado, K., Havemann, S., Labonnote, L.-C., Marenco, F. et al. (2014a) A self-consistent scattering model for cirrus. II: the high and low frequencies. *Quarterly Journal of the Royal Meteorological Society*, 140, 1039–1057. Available from: https://doi.org/10.1002/qj.2193

Baran, A.J. & Francis, P.N. (2004) On the radiative properties of cirrus cloud at solar and thermal wavelengths: a test of model consistency using high-resolution airborne radiance measurements. *Quarterly Journal of the Royal Meteorological Society*, 130, 763–778. Available from: https://doi.org/10.1256/qj.03.151

Baran, A.J., Furtado, K., Labonnote, L.-C., Havemann, S., Thelen, J.-C. & Marenco, F. (2015) On the relationship between the scattering phase function of cirrus and the atmospheric state. *Atmospheric Chemistry and Physics*, 15, 1105–1127. Available from: https://doi.org/10.5194/acp-15-1105-2015

Baran, A.J., Hill, P., Furtado, K., Field, P. & Manners, J. (2014b) A coupled cloud physics-radiation parameterization of the bulk optical properties of cirrus and its impact on the met Office unified model global atmosphere 5.0 configuration. *Journal of Climate*, 27, 7725–7752. Available from: https://doi.org/10.1175/JCLI-D-13-00700.1

Baran, A.J., Hill, P., Walters, D., Hardiman, S.C., Furtado, K., Field, P.R. et al. (2016) The impact of two coupled cirrus microphysics–radiation parameterizations on the temperature and specific humidity biases in the tropical tropopause layer in a climate model. *Journal of Climate*, 29, 5299–5316. Available from: https://doi.org/10.1175/JCLI-D-15-0821.1

Baran, A.J. & Labonnote, L.-C. (2006) On the reflection and polarisation properties of ice cloud. *Journal of Quantitative Spectroscopy & Radiative Transfer*, 100, 41–54.

Baran, A.J. & Labonnote, L.-C. (2007) A self-consistent scattering model for cirrus. 1: the solar region. *Quarterly Journal of the Royal Meteorological Society*, 133, 1899–1912.

Baum, B.A., Yang, P., Heymsfield, A.J., Schmitt, C.G., Xie, Y., Bansemer, A. et al. (2011) Improvements in shortwave bulk scattering and absorption models for the remote sensing of ice clouds. *Journal of Applied Meteorology and Climatology*, 50(5), 1037–1056.

Boucher, O., Randall, D., Artaxo, P., Bretherton, C., Feingold, G., Forster, P. et al. (2013) Clouds and aerosols. In: Stocker, T.F., Qin, D., Plattner, G.K., Tignor, M., Allen, S.K., Boschung, J. et al. (Eds.) *Climate change 2013: the physical science basis. Contribution of working group I to the fifth assessment report of the intergovernmental panel on climate change*. Cambridge, UK and New York: Cambridge Univ. Press, pp. 571–657.

Brown, P.R.A. & Francis, P.N. (1995) Improved measurements of the ice water content in cirrus using a Total-water probe. *Journal of Atmospheric and Oceanic Technology*, 12, 410–414.

Buriez, J.-C., Parol, F., Cornet, C. & Doutriaux-Boucher, M. (2005) An improved derivation of the top-of-atmosphere albedo from POLDER/ADEOS-2: narrowband albedos. *Journal of Geophysical Research*, 110, D05202. Available from: https://doi.org/10.1029/2004JD005243

Bush, M., Flack, D.L.A., Lewis, H.W., Bohnenstengel, S.I., Short, C.J., Franklin, C. et al. (2024) The third met Office unified model-JULES regional atmosphere and land configuration, RAL3. *Geoscientific Model Development Discussions*, 2024, 1–58. Available from: https://doi.org/10.5194/gmd-2024-201

Ceppi, P. & Nowack, P. (2021) Observational evidence that cloud feedback amplifies global warming. *Proceedings of the National Academy of Sciences of the United States of America*, 118(30), e2026290118.

Cooper, W.A. (1986) Ice initiation in natural clouds. In: *Precipitation enhancement—a scientific challenge. Meteorological monographs*. Boston, MA: American Meteorological Society. Available from: https://doi.org/10.1007/978-1-935704-17-1_4

Cotton, R.J., Field, P.R., Ulanowski, Z., Kaye, P.H., Hirst, E., Greenaway, R.S. et al. (2013) The effective density of small ice particles obtained from in situ aircraft observations of mid-latitude cirrus. *Quarterly Journal of the Royal Meteorological Society*, 139, 1923–1934. Available from: https://doi.org/10.1002/qj.2058

Edwards, J.M., Havemann, S., Thelen, J.C. & Baran, A.J. (2007) A new parametrization for the radiative properties of ice crystals: comparison with existing schemes and impact in a GCM. *Atmospheric Research*, 83(1), 19–35.

Edwards, J.M. & Slingo, A. (1996) A. Studies with a flexible new radiation code. I: choosing a configuration for a large-scale model. *Quarterly Journal of the Royal Meteorological Society*, 122, 689–719. Available from: https://doi.org/10.1002/qj.49712253107

Erfani, E. & Mitchell, D.L. (2016) Developing and bounding ice particle mass- and area-dimension expressions for use in atmospheric models and remote sensing. *Atmospheric Chemistry and Physics*, 16, 4379–4400. Available from: https://doi.org/10.5194/acp-16-4379-2016

Eriksson, P., Ekelund, R., Mendrok, J., Brath, M., Lemke, O. & Buehler, S.A. (2018) A general database of hydrometeor single scattering properties at microwave and sub-millimetre wavelengths. *Earth System Science Data*, 10(3), 1301–1326.

Field, P.R., Heymsfield, A.J. & Bansemer, A. (2007) Snow size distribution parameterization for midlatitude and tropical ice cloud. *Journal of the Atmospheric Sciences*, 64, 4346–4365. Available from: https://doi.org/10.1175/2007JAS2344.1

Field, P.R., Heymsfield, J., Bansemer, A. & Twohy, C.H. (2008) Determination of the combined ventilation factor and capacitance for ice crystal aggregates from airborne observations in a tropical anvil cloud. *Journal of the Atmospheric Sciences*, 65, 376–391.

Field, P.R., Hill, A., Shipway, B., Furtado, K., Wilkinson, J., Miltenberger, A. et al. (2023) Implementation of a double moment cloud microphysics scheme in the UK met Office regional numerical weather prediction model. *Quarterly Journal of the Royal Meteorological Society*, 149(752), 703–739. Available from: https://doi.org/10.1002/qj.4414

Foot, J.S. (1988) Some observations of the optical properties of clouds. II: cirrus. *Quarterly Journal of the Royal Meteorological Society*, 114(479), 145–164.

Francis, P.N. (1995) Some aircraft observations of the scattering properties of ice crystals. *Journal of Atmospheric Sciences*, 52(8), 1142–1154.

Fu, Q. (1996) An accurate parameterization of the solar radiative properties of cirrus clouds for climate models. *Journal of Climate*, 9, 2058–2082.

Furtado, K., Field, P.R., Cotton, R. & Baran, A.J. (2015) The sensitivity of simulated high clouds to ice crystal fall speed, shape and size distribution. *Quarterly Journal of the Royal Meteorological Society*, 141, 1546–1559. Available from: https://doi.org/10.1002/qj.2457

Furtado, K., Field, P.R., Luo, Y., Liu, X., Guo, Z., Zhou, T. et al. (2018) Cloud microphysical factors affecting simulations of deep convection during the presummer rainy season in southern China. *Journal of Geophysical Research: Atmospheres*, 123(18), 10–477. Available from: https://doi.org/10.1029/2017JD028192

Furtado, K., Tsushima, Y., Field, P.R., Rostron, J. & Sexton, D. (2023) The relationship between the present-day seasonal cycles of clouds in the mid-latitudes and cloud-radiative feedback. *Geophysical Research Letters*, 50(15), e2023GL103902.

Geiss, S., Scheck, L., de Lozar, A. & Weissmann, M. (2021) Understanding the model representation of clouds based on visible and infrared satellite observations. *Atmospheric Chemistry and Physics*, 21, 12273–12290. Available from: https://doi.org/10.5194/acp-21-12273-2021

Gordon, H., Field, P.R., Abel, S.J., Barrett, P., Bower, K., Crawford, I. et al. (2020) Development of aerosol activation in the double-moment unified model and evaluation with CLARIFY measurements. *Atmospheric Chemistry and Physics*, 20, 10997–11024. Available from: https://doi.org/10.5194/acp-20-10997-2020

Heymsfield, A.J., Bansemer, A., Schmitt, C., Twohy, C. & Poellot, M.R. (2004) Effective ice particle densities derived from aircraft data. *Journal of the Atmospheric Sciences*, 61, 982–1003.

Heymsfield, A.J., Schmitt, C., Bansemer, A. & Twohy, C.H. (2010) Improved representation of ice particle masses based on observations in natural clouds. *Journal of the Atmospheric Sciences*, 67, 3303–3318. Available from: https://doi.org/10.1175/2010JAS3507.1

Hill, A., Brown, N. & Shipway, B. (2018) Met Office/NERC Cloud Model (MONC): User Documentation. Technical Report, Met Office, UK.

Hill, A.A., Shipway, B.J. & Boutle, I.A. (2015) How sensitive are aerosol-precipitation interactions to the warm rain representation. *Journal of Advances in Modeling Earth Systems*, 7, 987–1004. Available from: https://doi.org/10.1002/2014MS000422

Hogan, R.J. & Bozzo, A. (2018) A flexible and efficient radiation scheme for the ECMWF model. *Journal of Advances in Modeling Earth Systems*, 10(8), 1990–2008.

Hogan, R.J. & Matricardi, M. (2022) A tool for generating fast k-distribution gas-optics models for weather and climate applications. *Journal of Advances in Modeling Earth Systems*, 14, e2022MS003033. Available from: https://doi.org/10.1029/2022MS003033

Hogan, R.J., Tian, L., Brown, P.R.A., Westbrook, C.D., Heymsfield, A.J. & Eastment, J.D. (2012) Radar scattering from ice aggregates using the horizontally aligned oblate spheroid approximation. *Journal of Applied Meteorology and Climatology*, 51, 655–671. Available from: https://doi.org/10.1175/JAMC-D-11-074.1

Hong, Y., Liu, G. & Li, J.L. (2016) Assessing the radiative effects of global ice clouds based on CloudSat and CALIPSO measurements. *Journal of Climate*, 29(21), 7651–7674.

IPCC. (2021) Climate change 2021: the physical science basis. In: Masson-Delmotte, V., Zhai, P., Pirani, A., Connors, S.L., Péan, C., Berger, S. et al. (Eds.) *Contribution of working group I to the sixth assessment report of the intergovernmental panel on climate change*. Cambridge, UK and New York: Cambridge University Press.

Jiang, X., Su, H., Jiang, J.H., Neelin, J.D., Wu, L., Tsushima, Y. et al. (2023) Muted extratropical low cloud seasonal cycle is closely linked to underestimated climate sensitivity in models. *Nature Communications*, 14, 5586.

Kleanthous, A., Baran, A.J., Betcke, T., Hewett, D.P. & Westbrook, C.D. (2024) An application of the boundary element method (BEM) to the calculation of the single-scattering properties of very complex ice crystals in the microwave and sub-millimetre regions of the electromagnetic spectrum. *Journal of Quantitative Spectroscopy and Radiative Transfer*, 312, 108793.

Korolev, A. & Isaac, G. (2003) Roundness and Aspect ratio of Particles in Ice Clouds. *Journal of the Atmospheric Sciences*, 60, 1795–1808.

Krämer, M., Rolf, C., Luebke, A., Afchine, A., Spelten, N., Costa, A. et al. (2016) A microphysics guide to cirrus clouds – part 1:

cirrus types. *Atmospheric Chemistry and Physics*, 16, 3463–3483. Available from: https://doi.org/10.5194/acp-16-3463-2016

Lawson, R.P., Woods, S., Jensen, E., Erfani, E., Gurganus, C., Gallagher, M. et al. (2019) A review of ice particle shapes in cirrus formed in situ and in anvils. *Journal of Geophysical Research*, 124, 10049–10090. Available from: https://doi.org/10.1029/2018JD030122

Leon, D.C. et al. (2016) The convective precipitation experiment (COPE): investigating the origins of heavy precipitation in the southwestern United Kingdom. *Bulletin of the American Meteorological Society*, 97(6), 1003–1020. Available from: https://doi.org/10.1175/BAMS-D-14-00157.1

Li, M., Letu, H., Peng, Y., Ishimoto, H., Lin, Y., Nakajima, T.Y. et al. (2022) Investigation of ice cloud modeling capabilities for the irregularly shaped Voronoi ice scattering models in climate simulations. *Atmospheric Chemistry and Physics*, 22(7), 4809–4825.

Liou, K.N. (1986) Influence of cirrus clouds on weather and climate processes: a global perspective. *Monthly Weather Review*, 114(6), 1167–1199.

Liu, C., Yang, P., Minnis, P., Loeb, N., Kato, S., Heymsfield, A. et al. (2014) A two-habit model for the microphysical and optical properties of ice clouds. *Atmospheric Chemistry and Physics*, 14, 13719–13737. Available from: https://doi.org/10.5194/acp-14-13719-2014

Loeb, N.G., Manalo-Smith, N., Su, W., Shankar, M. & Thomas, S. (2016) CERES top-of-atmosphere earth radiation budget climate data record: accounting for in-orbit changes in instrument calibration. *Remote Sensing*, 8(3), 182. Available from: https://doi.org/10.3390/rs8030182

Macke, A., Mueller, J. & Raschke, E. (1996) Single scattering properties of atmospheric ice crystal. *Journal of the Atmospheric Sciences*, 53, 2813–2825.

Manners, J., Edwards, J.M., Hill, P. & Thelen, J. (2023) SOCRATES (Suite Of Community RAdiative Transfer codes based on Edwards and Slingo) technical guide, Tech. rep., Met Office, UK. https://code.metoffice.gov.uk/trac/socrates

McCusker, K., Baran, A.J., Westbrook, C., Fox, S., Eriksson, P., Cotton, R. et al. (2024) The first microwave and submillimetre closure study using particle models of oriented ice hydrometeors to simulate polarimetric measurements of ice clouds. *Atmospheric Measurement Techniques*, 17, 3533–3552. Available from: https://doi.org/10.5194/amt-17-3533-2024

McFarquhar, G.M. & Heymsfield, A.J. (1998) The definition and significance of an effective radius for ice clouds. *Journal of the Atmospheric Sciences*, 55(11), 2039–2052.

McFarquhar, G.M., Iacobellis, S. & Somerville, R.C. (2003) SCM simulations of tropical ice clouds using observationally based parameterizations of microphysics. *Journal of Climate*, 16(11), 1643–1664.

Miltenberger, A.K., Field, P.R., Hill, A.A., Rosenberg, P., Shipway, B.J., Wilkinson, J.M. et al. (2018) Aerosol–cloud interactions in mixed-phase convective clouds – part 1: aerosol perturbations. *Atmospheric Chemistry and Physics*, 18, 3119–3145. Available from: https://doi.org/10.5194/acp-18-3119-2018

Mishchenko, M.I. & Travis, L.D. (1998) Capabilities and limitations of a current FORTRAN implementation of the T-matrix method for randomly oriented, rotationally symmetric scatterers. *Journal of Quantitative Spectroscopy & Radiative Transfer*, 60, 309–324.

Mitchell, D.L. (2002) Effective diameter in radiation transfer: general definition, applications, and limitations. *Journal of the Atmospheric Sciences*, 59(15), 2330–2346.

O'Shea, S., Crosier, J., Dorsey, J., Gallagher, L., Schledewitz, W., Bower, K. et al. (2021) Characterising optical array particle imaging probes: implications for small-ice-crystal observations. *Atmospheric Measurement Techniques*, 14, 1917–1939. Available from: https://doi.org/10.5194/amt-14-1917-2021

Ren, T., Li, D., Muller, J. & Yang, P. (2021) Sensitivity of radiative flux simulations to ice cloud parameterization over the equatorial western Pacific Ocean region. *Journal of the Atmospheric Sciences*, 78(8), 2549–2571.

Ren, T., Yang, P., Loeb, N.G., Smith, W.L., Jr. & Minnis, P. (2023) On the consistency of ice cloud optical models for spaceborne remote sensing applications and broadband radiative transfer simulations. *Journal of Geophysical Research: Atmospheres*, 128, e2023JD038747. Available from: https://doi.org/10.1029/2023JD038747

Rostron, J.W., Sexton, D.M., McSweeney, C.F., Yamazaki, K., Andrews, T., Furtado, K. et al. (2020) The impact of performance filtering on climate feedbacks in a perturbed parameter ensemble. *Climate Dynamics*, 55(3), 521–551.

Röttenbacher, J., Ehrlich, A., Müller, H., Ewald, F., Luebke, A.E., Kirbus, B. et al. (2024) Evaluating the representation of Arctic cirrus solar radiative effects in the integrated forecasting system with airborne measurements. *Atmospheric Chemistry and Physics*, 24(14), 8085–8104.

Shcherbakov, V., Gayet, J.-F., Baker, B. & Lawson, P. (2006) Light scattering by single natural ice crystals. *Journal of the Atmospheric Sciences*, 63, 1513–1525.

Sherwood, S.C., Webb, M.J., Annan, J.D., Armour, K.C., Forster, P.M., Hargreaves, J.C. et al. (2020) An assessment of Earth's climate sensitivity using multiple lines of evidence. *Reviews of Geophysics*, 58, e2019RG000678. Available from: https://doi.org/10.1029/2019RG000678

Shipway, B.J. & Hill, A.A. (2012) Diagnosis of systematic differ-ences between multiple parametrizations of warm rain micro-physics using a kinematic framework. *Quarterly Journal of the Royal Meteorological Society*, 138, 669.

Sieron, S.B., Clothiaux, E.E., Zhang, F., Lu, Y. & Otkin, J.A. (2017) Comparison of using distribution-specific versus effective radius methods for hydrometeor single-scattering properties for all-sky microwave satellite radiance simulations with different microphysics parameterization schemes. *Journal of Geophysical Research: Atmospheres*, 122(13), 7027–7046.

Sourdeval, O., Labonnote, L.-C., Baran, A.J. & Brogniez, G. (2015) A methodology for simultaneous retrieval of ice and liquid water cloud properties. Part I: information content and case-study. *Quarterly Journal of the Royal Meteorological Society*, 141, 870–882. Available from: https://doi.org/10.1002/qj.2405

Sourdeval, O., Labonnote, L.-C., Baran, A.J., Mülmenstädt, J. & Brogniez, G.A. (2016) Methodology for simultaneous retrieval of ice and liquid water cloud properties. Part 2: near-global retrievals and evaluation against A-train products. *Quarterly Journal of the Royal Meteorological Society*, 142, 3063–3081. Available from: https://doi.org/10.1002/qj.2889

Stocker, T.F., Qin, D., Plattner, G.K., Tingor, M., Allen, S.K., Boschung, J. et al. (2013) IPCC, 2013, climate change 2013: the physical science basis. In: *Contribution of working group I to the* *fifth assessment report of the intergovernmental panel on climate change*, Vol. 413. Berlin and Heidelberg: Cambridge Univ. Press.

Twomey, S. (1977) The influence of pollution on the shortwave albedo of clouds. *Journal of the Atmospheric Sciences*, 34, 1149–1152.

Walters, D., Baran, A.J., Boutle, I., Brooks, M., Earnshaw, P., Edwards, J. et al. (2019) The met Office unified model global atmosphere 7.0/7.1 and JULES global land 7.0 configurations. *Geoscientific Model Development*, 12, 1909–1963. Available from: https://doi.org/10.5194/gmd-12-1909-2019

Wang, Y. & Zhao, C. (2016) Can MODIS cloud fraction fully represent the diurnal and seasonal variations at DOE ARM SGP and Manus sites? *Journal of Geophysical Research. Atmospheres*, 122, 329–343. Available from: https://doi.org/10.1002/2016JD025954

Warren, S.G. & Brandt, R.E. (2008) Optical constants of ice from the ultraviolet to the microwave: a revised compilation. *Journal of Geophysical Research*, 113, D14220. Available from: https://doi.org/10.1029/2007JD009744

Westbrook, C.D., Ball, R.C., Field, P.R. & Heymsfield, A.J. (2004) Universality in snowflake aggregation. *Geophysical Research Letters*, 31(15), L15104.

Willmott, C.J. (1981) On the validation of models. *Physical Geography*, 2(2), 184–194. Available from: https://doi.org/10.1080/02723646.1981.10642213

Yang, H., Dobbie, S., Herbert, R., Connolly, P., Gallagher, M., Ghosh, S. et al. (2012) The effect of observed vertical structure, habits, and size distributions on the solar radiative properties and cloud evolution of cirrus clouds. *Quarterly Journal of the Royal Meteorological Society*, 138(666), 1221–1232.

Yang, P., Bi, L., Baum, B.A., Liou, K.N., Kattawar, G.W., Mishchenko, M.I. et al. (2013) Spectrally consistent scattering, absorption, and polarization properties of atmospheric ice crystals at wavelengths from 0.2 to 100 μm. *Journal of the Atmospheric Sciences*, 70(1), 330–347.

Yang, P. & Liou, K.N. (1998) An efficient algorithm for truncating spatial domain in modeling lighting scattering by finite-difference technique. *Journal of Computational Physics*, 140, 346–369.

Yang, P., Liou, K.N., Bi, L., Liu, C., Yi, B. & Baum, B.A. (2015) On the radiative properties of ice clouds: light scattering, remote sensing, and radiation parameterization. *Advances in Atmospheric Sciences*, 32, 32–63.

Yi, B., Yang, P., Baum, B.A., L'Ecuyer, T., Oreopoulos, L., Mlawer, E.J. et al. (2013) Influence of ice particle surface roughening on the global cloud radiative effect. *Journal of the Atmospheric Sciences*, 70, 2794–2807.

Zhang, Y., Macke, A. & Albers, F. (1999) Effect of crystal size spectrum and crystal shape on stratiform cirrus radiative forcing. *Atmospheric Research*, 52(1–2), 59–75.

Zhao, W., Peng, Y., Wang, B., Yi, B., Lin, Y. & Li, J. (2018) Comparison of three ice cloud optical schemes in climate simulations with community atmospheric model version 5. *Atmospheric Research*, 204, 37–53.

Zhou, Y., Liu, Y., Han, W., Zeng, Y., Sun, H., Yu, P. et al. (2024) Exploring the characteristics of Fengyun-4A advanced geostationary radiation imager (AGRI) visible reflectance using the China Meteorological Administration mesoscale (CMA-MESO) forecasts and its implications for data assimilation. *Atmospheric Measurement Techniques*, 17(22), 6659–6675.

SUPPORTING INFORMATION

Additional supporting information can be found online in the Supporting Information section at the end of this article.

How to cite this article: Baran, A.J., Manners, J., Field, P.R., Furtado, K. & Hill, A. (2025) A consistent coupling of two-moment microphysics and bulk ice optical properties, and its impact on radiation in a regional weather model. *Quarterly Journal of the Royal Meteorological Society*, e5025. Available from: https://doi.org/10.1002/qj.5025